

# Constraints on Radial Migration in Spiral Galaxies - II. Angular momentum distribution and preferential migration

Kathryne J. Daniel<sup>1,2\*</sup> and Rosemary F. G. Wyse<sup>2,3</sup>

<sup>1</sup>*Department of Physics, Bryn Mawr College, Bryn Mawr, PA 19010, USA*

<sup>2</sup>*Department of Physics & Astronomy, Johns Hopkins University, Baltimore, MD 21218, USA*

<sup>3</sup>*Institute for Astronomy, University of Edinburgh, Blackford Hill, Edinburgh EH9 3HJ, Scotland, UK*

Accepted January 20, 2018. Received January 3, 2018; in original form October 30, 2017

## ABSTRACT

The orbital angular momentum of individual stars in galactic discs can be permanently changed through torques from transient spiral patterns. Interactions at the corotation resonance dominate these changes and have the further property of conserving orbital circularity. We derived in an earlier paper an analytic criterion that an unperturbed stellar orbit must satisfy in order for such an interaction to occur i.e. for it to be in a trapped orbit around corotation. We here use this criterion in an investigation of how the efficiency of induced radial migration for a population of disc stars varies with the angular momentum distribution of that population. We frame our results in terms of the velocity dispersion of the population, this being an easier observable than is the angular momentum distribution. Specifically, we investigate how the fraction of stars in trapped orbits at corotation varies with the velocity dispersion of the population, for a system with an assumed flat rotation curve. Our analytic results agree with the finding from simulations that radial migration is less effective in populations with ‘hotter’ kinematics. We further quantify the dependence of this trapped fraction on the strength of the spiral pattern, finding a higher trapped fraction for higher amplitude perturbations.

**Key words:** galaxies: evolution, galaxies: kinematics and dynamics, galaxies: structure

## 1 INTRODUCTION

Internal, secular mechanisms can have a significant impact on the evolution of galactic discs (see e.g. Sellwood 2014). For example, it is now recognized that disc stars can migrate radially, moving of order a disc scale-length over their lifetime, through successive resonant interactions with transient gravitational perturbations (for observational evidence, see e.g., Wielen et al. (1996); Bovy et al. (2012); Radburn-Smith et al. (2012); Hayden et al. (2015); Kordopatis et al. (2015); Loebman et al. (2016) and for theoretical investigations see e.g. Sellwood & Binney (2002); Roškar et al. (2008); Schönrich & Binney (2009); Loebman et al. (2011); Minchev et al. (2012); Roškar et al. (2013); Vera-Ciro et al. (2016); Martinez-Medina et al. (2017); Peschken et al. (2017); Schönrich & McMillan (2017)). Lynden-Bell & Kalnajs (1972) established that stars on close to circular orbits can exchange orbital angular momentum with steady (or slowly growing) spiral waves at the major resonances, namely corotation and the inner/outer Lindblad resonances. These authors further demonstrated that the change in angular momentum at corotation occurs without any increase in the energy associated with non-circular motion, whereas torques at the Lindblad resonances do increase orbital eccentricity (i.e. cause kinematic heating of the population).

Sellwood & Binney (2002), in an influential paper, showed that for a star in a “trapped orbit”<sup>1</sup> around the corotation radius of a *transient* spiral pattern, the angular momentum change can be permanent, leading to radial migration of the star.

\* E-mail: kjdaniel@brynmawr.edu

<sup>1</sup> We use the term “trapped orbit” for members of the “horseshoe” orbital family associated with the corotation resonance, in order to emphasise their role as the first stage in radial migration.

While the spiral pattern exists, a trapped star is repeatedly torqued, causing its mean orbital radius (hereafter denoted  $R_L$ , under the assumption that it equals the guiding centre radius in the epicyclic approximation, i.e. the radius of a circular orbit with angular momentum equal to that of the star at that instant) to move outwards then inwards across corotation. The star's guiding centre radius oscillates in time until the torques cease when the transient spiral perturbation dies away, restoring axisymmetry and leaving the star with a new value for orbital angular momentum and guiding radius (except in the unlikely case that it is dropped back where it started). There is no associated increase in non-circular motion. Sellwood & Binney (2002) showed that interactions at the corotation resonance dominate the angular momentum changes in the disc (compared to interactions at the Lindblad resonances). We will refer to the changes in mean orbital radius due to the corotation interactions as “radial migration”.

All orbits have an associated circular frequency and so, provided there exists an appropriately matched spiral (with pattern speed approximately equal to the stars's circular frequency) for a long enough period of time, any star could in principle migrate radially. However, as pointed out by Sellwood & Binney (2002), stars on eccentric orbits cannot “keep station” with the spiral pattern at the radius of corotation and therefore radial migration is expected to be less important for kinematically hotter stellar populations. Our investigations in this paper are aimed at quantifying this expectation.

We earlier (Daniel & Wyse 2015, hereafter Paper I) derived an analytic expression for a “capture criterion” that determines whether or not a disc star with given instantaneous 4D phase-space coordinates may be in a trapped orbit around the corotation radius of an imposed spiral pattern (see Appendix A for a brief review). The physical interpretation of this capture criterion (given in equation A7) is that the orbital angular momentum of a star is the most important quantity that determines whether or not that star is in a trapped orbit. Indeed, the criterion may be re-stated for kinematically warmed stellar orbits, where such a star will be in a trapped orbit provided the instantaneous value of its guiding centre radius lies within a certain region, the “capture region” surrounding the corotation radius. This capture region is approximately delineated by the closed contours of the effective potential ( $\Phi_{eff}$ , the potential in the frame that rotates with the spiral pattern) (see Daniel & Wyse 2015, §2.2.1 for a more complete description). The capture regions for three different strengths of spiral perturbation are illustrated in Figure 1, as shaded areas outlined with a thick, black line (see Table 1 for the values of the fixed parameters of the model; the radius of corotation is here chosen to be at  $R_{CR} = 8$  kpc). Contours of the effective potential are shown by thin lines while the local maxima in the surface density of the spiral pattern are indicated by thick, dashed (magenta) curves. The maximum radial extent of the capture region equals the maximum possible change in guiding center radius - and hence distance of induced radial migration - from the given (transient) spiral pattern. This maximum width equals a few kiloparsec, of order the disc scale-length, for the parameter values chosen for Figure 1. Most stars will migrate significantly less than the maximum distance (quantified in Daniel & Wyse 2018).

Circular orbits do not exist in a non-axisymmetric potential due to non-conservation of angular momentum. We can however consider a star moving on an orbit along which, at all times, the (time-dependent) spatial coordinates of the guiding centre equal those of the star (its orbit has zero random energy). In this case, should the star be in a trapped orbit, it is physically located within the capture region. A star on an orbit with finite random energy meets the capture criterion and is in a trapped orbit provided its *guiding centre* is within the capture region, even while the star's spatial coordinates place it outside the capture region. The typical amplitude of radial epicyclic excursions for a population of stars with radial velocity dispersion  $\sigma_R$ , moving in a potential with local epicyclic frequency  $\kappa$ , may be approximated by the ratio  $\sigma_R/\kappa$ . Stars in the local Galactic disc with  $\sigma_R \sim 30 \text{ km s}^{-1}$  have excursions of order 1 kpc. Taking the finite width of the capture region into account, for the model of panel (a) Figure 1, stars that are members of such a population physically located  $\gtrsim 2$  kpc from corotation could meet the capture criterion (guiding centre within the capture region). Further, for a flat rotation curve the epicyclic frequency decreases with radial coordinate as  $\kappa \propto R^{-1}$  so that for given value of velocity dispersion, the epicyclic excursions are larger in the outer disc and stars located further from corotation can meet the capture criterion.

The radial period of trapped orbits for a given spiral perturbation is longer for larger excursions.<sup>2</sup> Our numerical experiments show that the largest trapped orbits have periods a few times longer than a galactic year at corotation. A trapped orbit that has guiding centre excursions of order  $\sim 1$  kpc from corotation, in the potential illustrated by Figure 1, panel(a), takes  $\sim 8 \times 10^8$  years to complete a full radial oscillation, whereas a galactic year at corotation is  $\sim 2.2 \times 10^8$  years and the epicyclic period is  $\sim 1.6 \times 10^8$  years. The radial period of trapped orbits with the largest excursions places a lower limit on the timescale for full phase mixing of trapped orbits around corotation. Therefore the minimum lifetime for a transient spiral that can induce radial migration over a significant distance is a few times a galactic year at corotation.

In this paper, we apply the capture criterion to a series of model disc galaxies with the aim of determining the (initial) distribution and fraction of a population of stars in trapped orbits due to an imposed spiral pattern.<sup>3</sup> While orbital angular momentum is the physical parameter that is most important in determining whether or not a star meets the capture criterion, the orbital angular momentum distribution is far from trivial to determine from observations. We therefore use velocity

<sup>2</sup> Simple harmonic motion is not a good approximation for trapped orbits (see, for example, Contopoulos 1973).

<sup>3</sup> We do not include possible additional perturbations to the gravitational potential, such as a bar or Giant Molecular Clouds, that could scatter stars out of trapped orbits associated with the spiral of interest.

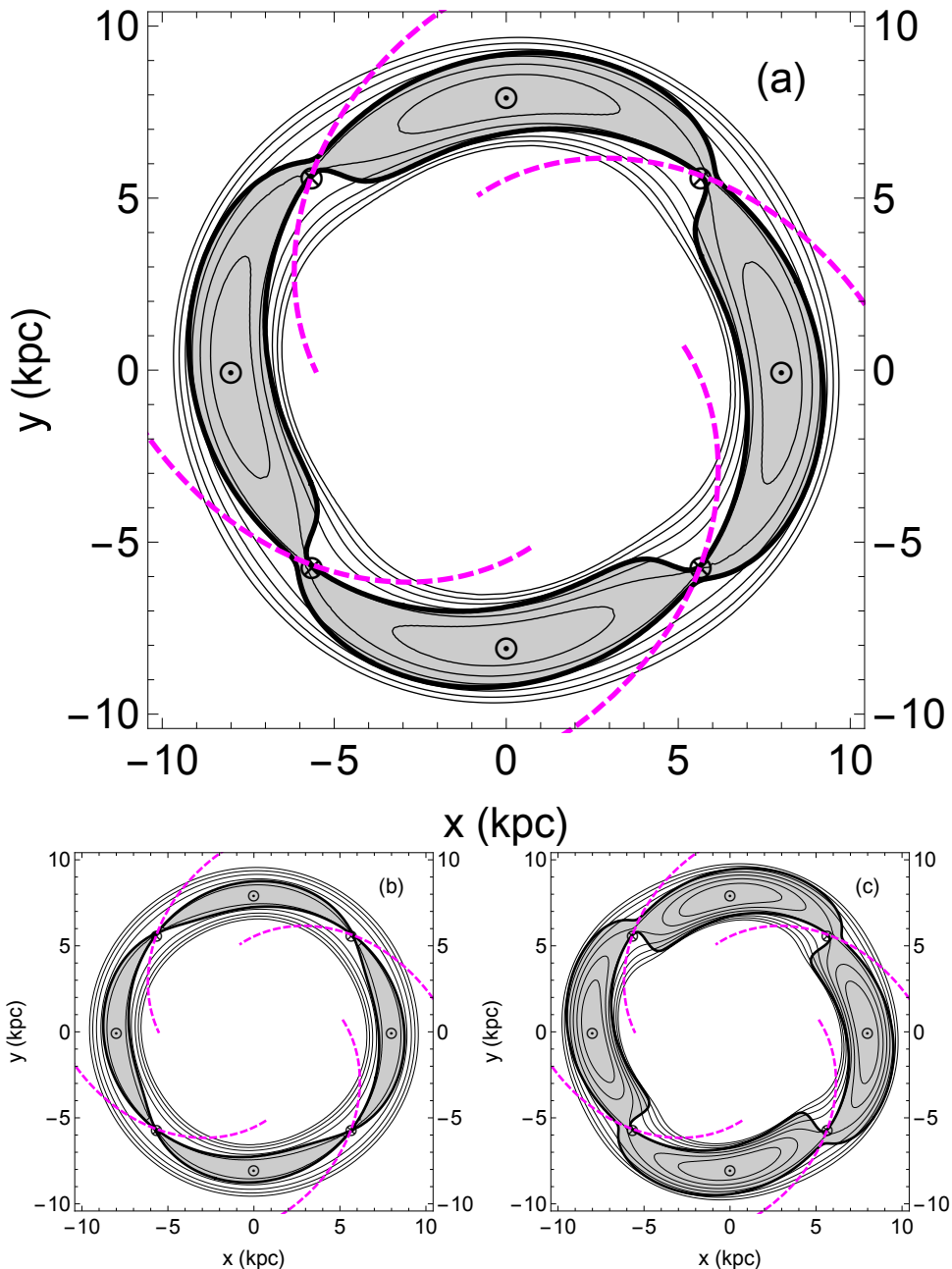


**Figure 1.** Contours of the effective potential,  $\Phi_{eff}$ , for a trailing spiral pattern with fixed parameter values given in Table 1, radius of corotation at  $R_{CR} = 8$  kpc, and fractional amplitude for the spiral surface density equal to  $\epsilon_{\Sigma} = 0.3$  in panel (a),  $\epsilon_{\Sigma} = 0.1$  in panel (b), and  $\epsilon_{\Sigma} = 0.5$  in panel (c). Contours are shown in  $400 \text{ km}^2 \text{ s}^{-2}$  intervals around the value of  $\Phi_{eff}$  at the peak amplitude of the spiral pattern and are within 2 kpc of corotation. The locations of the peaks of the spiral perturbation are shown as thick, dashed (magenta) curves. The local maxima in  $\Phi_{eff}$  (located between the spiral arms) are marked with the symbol  $\odot$  and the saddle points (the deepest part of the spiral potential at  $R = R_{CR}$ ) are marked with  $\otimes$  (note these are on the magenta dashed curves marking the maxima of the spiral pattern). The capture region has a thick (black) outline and is shaded grey. The model shown in panel (a) is adopted for much of the analysis in this paper.

dispersion as a proxy. Our analysis aims to quantify how the velocity dispersion of a population determines the fraction of disc stars that satisfy the capture criterion.

This paper is organized as follows: we outline our approach in §2, with the adopted two-dimensional disc potentials described in §2.1, the analytic forms of the stellar phase-space distribution functions in §2.2, and derive the resulting distribution of orbital angular momentum for each model in §2.3. We apply our capture criterion to simple versions of these models in §3 in order to focus on how the trapped population depends on both invariant and radially varying forms of the stellar velocity dispersion in §3.1 and §3.2, respectively. We investigate how the trapped population depends on other parameters of the model

**Table 1.** Adopted parameter values when a quantitative analysis is required, unless otherwise stated.

Parameter	Symbol	Value
Circular velocity (assumed constant with radius)	$v_c$	220 km s <sup>-1</sup>
Characteristic scale of underlying potential	$R_p$	1 kpc
Number of spiral arms	$m$	4
Spiral pitch angle	$\theta$	25°
Fractional amplitude of spiral surface density	$\epsilon_\Sigma$	0.3
Disc surface density normalisation	$\Sigma(R = 8 \text{ kpc})$	50 M <sub>⊙</sub> pc <sup>-2</sup>
Scale length for surface density	$R_d$	2.5 kpc
Radial width of an annulus	$\delta R$	0.1 kpc

(such as strength of the assumed spiral) in §3.3. We apply our capture criterion to the full models of the Galactic disc in §4. §5 places our results in the context of earlier investigations and §6 summarises our conclusions. The Appendix contains a short discussion of the salient points in the derivation of the analytic capture criterion from Paper I.

## 2 APPROACH

This section describes our models for the potential of the disc, the stellar kinematics, and the spatial distribution of stars. We will consider only motion in the equatorial plane of an underlying axisymmetric potential (plus imposed spiral perturbation). Unless otherwise stated, we use the values given in Table 1 when quantitative calculations are required.

### 2.1 Model for the Disc Potential

We assume that the potential governing the motion within an infinitely thin disc,  $\Phi(R, \phi)$  in cylindrical coordinates, results from an underlying axisymmetric potential,  $\Phi_0(R)$ , plus a spiral perturbation that is time-dependent in the inertial frame,  $\Phi_1(R, \phi, t)$ . We adopt the logarithmic axisymmetric potential that gives rise to a flat rotation curve,

$$\Phi_0(R) = v_c^2 \ln(R/R_p), \quad (1)$$

where  $v_c$  is the (constant) circular velocity and  $R_p$  is the characteristic scale of the potential. We superpose an  $m$ -armed spiral density wave<sup>4</sup> (Lin & Shu 1964; Lin et al. 1969; Binney & Tremaine 2008) of the form

$$\Phi_1(R, \phi) = |\Phi_s(R)| \cos[m \cot \theta \ln(R/R_{CR}) - m \phi] \quad (2)$$

in the (non-inertial) frame rotating with the spiral pattern speed ( $\Omega_p$ ).  $R_{CR} = v_c/\Omega_p$  is the radius of corotation and  $\theta$  is the pitch angle of the spiral arm (measured counter-clockwise from a line of constant azimuth). The zero of the azimuthal coordinate,  $\phi$ , may be chosen arbitrarily and for convenience we chose it to be at the maximum of  $\Phi_{eff}$  aligned with the positive  $x$ -axis in Figure 1. Further,  $\phi$  increases in the counter-clockwise direction.

The amplitude of the spiral potential of equation 2 is given by

$$\Phi_s(R) = \frac{2\pi G \Sigma(R) \epsilon_\Sigma}{k(R)}, \quad (3)$$

where  $\Sigma(R)$  is the surface density of the disc,  $\epsilon_\Sigma$  is the fractional amplitude in surface density of the spiral pattern, and  $k(R)$  is the radial wavenumber of the spiral pattern, defined as:

$$k(R) = \frac{m}{R \tan \theta}. \quad (4)$$

This form for the spiral potential has a radially dependent amplitude ( $\Phi_s(R)$ ) for any given fractional enhancement in surface density ( $\epsilon_\Sigma$ ). Further, the radius of corotation enters explicitly (see equation 2); we return to these points in §3.3 below.

### 2.2 Models for the Kinematics of the Axisymmetric Disc

We adopt two different prescriptions for the stellar phase space distribution function,  $f$ , to facilitate exploration of the role of the angular momentum distribution. The first assumes simple Gaussians for each component of motion, while the second, taken from Dehnen (1999), produces an asymmetric azimuthal-velocity distribution, with a tail to lower values (matching observations in the local disc). We assume that the phase space distribution is unchanged during the turn-on of the spiral pattern (discussed in the introduction to §3).

<sup>4</sup> We assume a density wave for two reasons: its form is analytic and the pattern speed is invariant with radius.

### 2.2.1 Gaussian Velocity Distribution

The 4D phase space distribution function for 2D motion in the disc plane can be written in the form (the 6D form is given by Binney & Tremaine 2008, equation 4.22),

$$f(\mathbf{x}, \mathbf{v}) = \Sigma(\mathbf{x}) P(\mathbf{v})_{\mathbf{x}}, \quad (5)$$

where  $P(\mathbf{v})_{\mathbf{x}}$  is the velocity distribution function at coordinate  $\mathbf{x}$  and  $\Sigma(\mathbf{x})$  is the surface density of the disc. We assume that the disc follows an exponential surface density profile (e.g., Freeman 1970):

$$\Sigma(R) = \Sigma_0 e^{-R/R_d}, \quad (6)$$

with radial scale length  $R_d$ .

The velocity distribution function may be approximated by a 2D Gaussian, which we will denote by  $P_G(\mathbf{v})_{\mathbf{x}}$ . This form cannot reproduce the observed non-Gaussian skew in the azimuthal velocities at a given location in the disc, so in our models below that adopt the Gaussian, asymmetric drift is incorporated by a simple offset in the mean.

We decompose the velocity (in the inertial frame) into circular velocity plus random velocity:

$$\begin{aligned} \mathbf{v} &= v_R \hat{\mathbf{R}} + v_\phi \hat{\phi} \\ &= v_{ran,R} \hat{\mathbf{R}} + (v_c + v_{ran,\phi}) \hat{\phi} \\ &= \mathbf{v}_{ran} + \mathbf{v}_c. \end{aligned} \quad (7)$$

The distribution of the radial component of the (random) velocity is centred on  $\langle v_{ran,R} \rangle = 0$ , with standard deviation equal to the assumed radial velocity dispersion,  $\sigma_R(\mathbf{x})$ . The azimuthal velocity distribution is centred at  $v_c + \langle v_{ran,\phi} \rangle \equiv v_c - v_a$ , where  $v_a$  is the asymmetric drift. As discussed in Binney & Tremaine (2008) (their sections 4.4.3 and 4.8.2a), for any distribution function that represents a kinematically cool disc (i.e. the random motions are much less than the circular velocity), the asymmetric drift velocity scales approximately as the square of the radial velocity dispersion. Our models are intended to resemble the Milky Way disc and we adopt the following relation, consistent with local observations and with the (simplified) radial Jeans equation evaluated for the solar location (Dehnen & Binney 1998):

$$v_a = \sigma_R^2/C, \quad (8)$$

where the scaling constant is set to  $C = 80 \text{ km s}^{-1}$ .

We further simplify the analysis by assuming a fixed ratio of radial to azimuthal velocity dispersions, equal to that obtained for the local disc,  $\sigma_R/\sigma_\phi = 0.63$  (Nordström et al. 2004) (which is very similar to the value of  $1/\sqrt{2}$  expected for a flat rotation curve; Binney & Tremaine (2008, equation 3.100)). This allows us to express the 2D probability distribution for velocity at a given spatial coordinate in terms of the radial velocity dispersion alone, as:

$$\begin{aligned} P_G(\mathbf{v})_{\mathbf{x}} &= \frac{1}{2\pi\sigma_R\sigma_\phi} \exp \left\{ -\frac{(v_R - \langle v_R \rangle)^2}{2\sigma_R^2} - \frac{(v_\phi - \langle v_\phi \rangle)^2}{2\sigma_\phi^2} \right\} \\ &= \frac{0.63}{2\pi\sigma_R^2(R)} \exp \left\{ -\frac{v_{ran,R}^2}{2\sigma_R^2(R)} - \frac{(v_{ran,\phi} + \sigma_R^2(R)/C)^2}{2(\sigma_R(R)/0.63)^2} \right\}, \end{aligned} \quad (9)$$

where we have explicitly indicated that the radial velocity dispersion may vary with radial coordinate. The positive sign in front of the asymmetric drift term of the exponential in the second row of equation 9 sets the mean azimuthal velocity to slower rotation for kinematically hotter populations. Populations with different prescriptions for  $\sigma_R$  will also have different orbital angular momentum distributions (and hence different fractions of stars in trapped orbits, for given imposed spiral pattern). This is discussed in more detail in §2.3 below.

The full Gaussian distribution function we adopt in two of the models investigated below thus has the form

$$\begin{aligned} f_G(\mathbf{x}, \mathbf{v}) &= \Sigma(\mathbf{x}) P_G(\mathbf{v})_{\mathbf{x}} \\ &= \Sigma_0 e^{-R/R_d} \frac{0.63}{2\pi\sigma_R^2(R)} \exp \left\{ -\frac{v_{ran,R}^2}{2\sigma_R^2(R)} - \frac{(v_{ran,\phi} + \sigma_R^2(R)/C)^2}{2(\sigma_R(R)/0.63)^2} \right\}. \end{aligned} \quad (10)$$

### 2.2.2 Distribution Function for a Warmed Disc

The distribution function for an axisymmetric stellar disc with finite random motions may be obtained by ‘warming’ the distribution function for an initially cold disc (where all stars are on circular orbits). This approach was pioneered by Shu (1969) and revisited by Dehnen (1999). In these warmed-disc distribution functions, the radial excursions of stars on non-circular orbits from the inner disc naturally give rise to asymmetric drift and a low velocity tail in the azimuthal velocity distribution (Shu 1969). There are several choices for the form of the warmed-disc distribution function and we adopt that given as  $f_{new}$  in Dehnen (1999, his equation (10)), which we denote  $f_D$ :

$$f_D(E, L_z) = \frac{\Sigma(R_E)}{\sqrt{2\pi\sigma_R^2(R_E)}} \exp \left\{ \frac{\Omega(R_E)[L_z - L_c(R_E)]}{\sigma_R^2(R_E)} \right\}, \quad (11)$$

**Table 2.** Important parameters for the models presented in §3.2.

Model Name	$DF$	$\sigma_R(R)$	$R_\sigma$	Normalisation Value $\sigma_R(R = 8 \text{ kpc})$
Model $\Sigma$	$f_G$	$\propto \Sigma^{1/2}$	$2R_d$	$35 \text{ km s}^{-1}$
Model Q	$f_G$	$\propto R e^{-R/R_\sigma}$	$R_d$	$28 \text{ km s}^{-1}$
Model W	$f_D$	$\propto e^{-R/R_\sigma}$	$3R_d$	$35 \text{ km s}^{-1}$

where  $E$  is orbital energy, which enters the right-handside through the parameter  $R_E$  which is the orbital radius for a star in a circular orbit with energy  $E$ ,  $\Omega(R)$  is the circular frequency at a given radial coordinate,  $L_z$  represents orbital angular momentum (about the  $z$ -axis) and  $L_c(R)$  is the orbital angular momentum of a star in a circular orbit at radius  $R$ . The surface density generated from  $f_D$  is well approximated by an exponential at radii greater than a disc scale length (Dehnen 1999).

### 2.2.3 Prescriptions for the Radial Velocity Dispersion Profile

We explore two different types of prescription for the radial velocity dispersion profile, with two different aims. The first, adopted in the analyses of sections §3.1 and §3.3, assumes a constant velocity dispersion, independent of radial coordinate. This assumption allows us to estimate how the kinematic temperature affects the fraction of stars in trapped orbits (after imposition of a spiral pattern), and particularly to isolate and evaluate the effects of asymmetric drift (equation 8). Since stellar velocity dispersions are observed to vary with radius, this first approach is valid only when applied over a limited radial range. This leads to our second approach, adopting different forms of the possible variation of velocity dispersion with radius. We investigate the results from three specific radial velocity dispersion profiles (detailed in Table 2) in sections §3.2 and §4.

Table 2 also gives the form of the adopted velocity distribution function for three fiducial models (denoted  $\Sigma$ , Q and W). Model  $\Sigma$  incorporates the form of  $\sigma_R(R)$  that is appropriate for a locally isothermal, self gravitating disc with scale height independent of radius and with fixed ratio of  $\sigma_R/\sigma_z$ , namely  $\sigma_R^2(R) \propto \Sigma(R)$  (van der Kruit & Searle 1981; Lewis & Freeman 1989). For an assumed exponential surface density profile,  $\sigma_R(R) = \sigma_{R,0} e^{-R/R_\sigma}$ , where  $R_\sigma = 2R_d$ . As noted in Table 2, the radial velocity dispersion is normalised such that  $\sigma_R(R = 8 \text{ kpc}) = 35 \text{ km s}^{-1}$ , in order to approximate solar neighbourhood values. In this model (Model  $\Sigma$ ), we adopt a Gaussian distribution function,  $f_G$ , which includes the prescription for asymmetric drift given by equation 8.

Model Q also uses the Gaussian velocity distribution function ( $f_G$ ) and the prescription for asymmetric drift (equation 8). The velocity dispersion profile, however, is determined by setting the Toomre Q parameter (Toomre 1964) for local stellar disc stability to 1.5 at all radii,

$$Q \equiv \frac{\sigma_R(R) \kappa(R)}{3.36 G \Sigma(R)} = 1.5. \quad (12)$$

Such a kinematically warm disc is locally stable but may support global instabilities at all radii (see Sellwood 2014). We are interested in modelling a disc that could have transient instabilities at any radius. Sellwood & Carlberg (2014) found that transient *modes* can occur in their N-body simulations even as the disc is heated to  $Q > 1.5$  by spiral activity. In a disc with a flat rotation curve,  $\kappa(R) \propto R^{-1}$  so that  $\sigma_R(R) \propto R e^{-R/R_d}$  for constant  $Q$ . We normalise the model by setting the surface density at  $R = 8 \text{ kpc}$  equal  $50 M_\odot \text{ pc}^{-2}$  (Table 1) in order to approximate the local disc (Kuijken & Gilmore 1991).

Model W is constructed under the assumption of a kinematically warmed disc using the modified Shu distribution function  $f_D$  introduced in section 2.2.2. Dehnen (1999) found that the radial velocity dispersion profile derived from the second moments of  $f_D$  is well approximated by an exponential radial profile such that  $\sigma_R(R) = \sigma_{R,0} e^{-R/R_\sigma}$ , with  $R_\sigma = 3R_d$ . Unless otherwise noted, the value of  $\sigma_{R,0}$  is again normalised such that the radial velocity dispersion  $\sigma_R(R = 8 \text{ kpc}) = 35 \text{ km s}^{-1}$ .

The radial profiles for  $\sigma_R(R)$  for each of these three prescriptions are illustrated in Figure 2. The curves show Model  $\Sigma$  (dashed, blue), Model Q (thick, red), and Model W (dot-dashed, black), normalised as in Table 1. We also show estimated values for the Milky Way disc from observations of K-giant stars (green, circles; Lewis & Freeman (1989) and thin disc stars from the RAVE survey (magenta, squares) (Pasetto et al. 2012). The  $Q = 1.5$  curve lies below the data for much of the disc, implying that the adopted normalisation is not well-matched to the Milky Way. This does not affect the *trends that are the main focus of our investigation*.

The capture criterion (equation A6) was derived using the epicyclic approximation and thus implicitly assumes small amplitude random motions. We established the validity of this criterion for any single component of stellar random velocity up to  $\sim 50 \text{ km s}^{-1}$  (Daniel & Wyse 2015) but we did not test it above this value. We therefore use thick/thin lines to distinguish these two regimes in Figure 2 and subsequent figures.

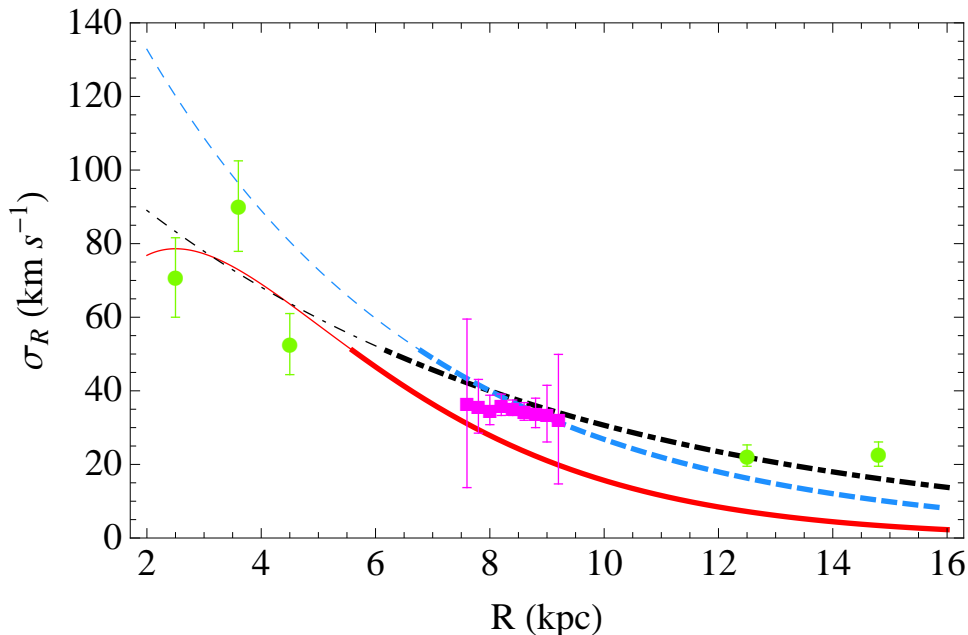


**Figure 2.** The radial velocity dispersion profiles of the three models outlined in Tables 1 and 2. The curves represent  $\sigma_R \propto \Sigma(R)^{1/2} \propto e^{-R/2R_d}$  (Model  $\Sigma$  - dashed, blue),  $\sigma_R \propto e^{-R/3R_d}$  (Model W - dot-dashed, black), and  $\sigma_R(R) \propto R e^{-R/R_d}$  normalised so that  $Q = 1.5$  (Model Q - thick, red) for a flat rotation curve. For reference, we have plotted data for the Milky Way disc for K-giant stars (green, circles) (Lewis & Freeman 1989) and for thin disc stars from the RAVE survey (selected based on kinematics and location from the plane  $-0.5 < z(\text{kpc}) \leq -0.3$ ; magenta, squares) (Pasetto et al. 2012). Thinner line types indicate a radial velocity dispersion  $\sigma_R > 50 \text{ km s}^{-1}$ , where the epicyclic approximation may break down and we have not tested our capture criterion.

### 2.3 Orbital Angular Momentum Distributions

The distribution of orbital angular momentum in the disc plays a critical role in determining which stars can be in trapped orbits, and in this section we evaluate this distribution for each of our models<sup>5</sup>.

We assume for models  $\Sigma$  and W that a population characterised by radial velocity dispersion  $\sigma_R$  at radius  $R$  will have a mean azimuthal velocity  $\langle v_\phi \rangle$  that lags the circular orbital velocity by  $v_a$  (equation 8) and mean guiding centre radius interior to  $R$ .

We calculate the radial distribution of orbital angular momentum by dividing the disc into annuli of width  $\delta R$  and evaluating the angular momentum content in each annulus as follows:

$$L_z(R_i) = \int_{-\infty}^{\infty} \int_{-\infty}^{\infty} \int_0^{2\pi} \int_{R_i}^{R_i+\delta R} R v_\phi f(\mathbf{x}, \mathbf{v}) R dR d\phi dv_R dv_\phi, \quad (13)$$

where we have assumed that all stars have unit mass (for an individual star,  $L_{z,*} = R_* v_{\phi,*}$ ). The orbital angular momentum in each annulus of an exponential disc with a flat rotation curve that is entirely composed of stars in circular orbits is given by,

$$L_{z,c}(R_i) = 2\pi v_c \int_{R_i}^{R_i+\delta R} \Sigma(R) R^2 dR. \quad (14)$$

The radial distribution of orbital angular momentum,  $L_z(R_i)$ , for each model of Table 2 is shown in Figure 3, normalised in each annulus by the corresponding purely circular orbit model ( $L_{z,c}(R_i)$ ). In adopting this normalisation we are implicitly assuming that the integral of each distribution function over velocity space gives a surface density profile that is well approximated by an exponential (equation 6). The line types in Figure 3 correspond to those in Figure 2, and again thin lines represent regions where the radial velocity dispersion  $\sigma_R > 50 \text{ km s}^{-1}$  and underlying assumptions may be expected to break down.

The radial profile for the mean orbital angular momentum goes as  $\langle L_z(R) \rangle \propto R \Sigma(R) \langle v_\phi(R) \rangle$ , where  $\langle v_\phi(R) \rangle$  is the mean azimuthal velocity of the stars at radial coordinate  $R$ . The radial Jeans equations show that for a given scalelength, populations that have higher random orbital energy have lower azimuthal streaming velocity (see §3.1 for a brief discussion).

<sup>5</sup> The distribution of orbital angular momentum in the disc may be rearranged at some later time. However, Sellwood & Binney (2002) and Sellwood (2014) argue that the net change in the orbital angular momentum distribution due to radial migration is nearly zero for any distribution function that has a shallow gradient in orbital angular momentum,  $\partial f / \partial L_z$ , near corotation.

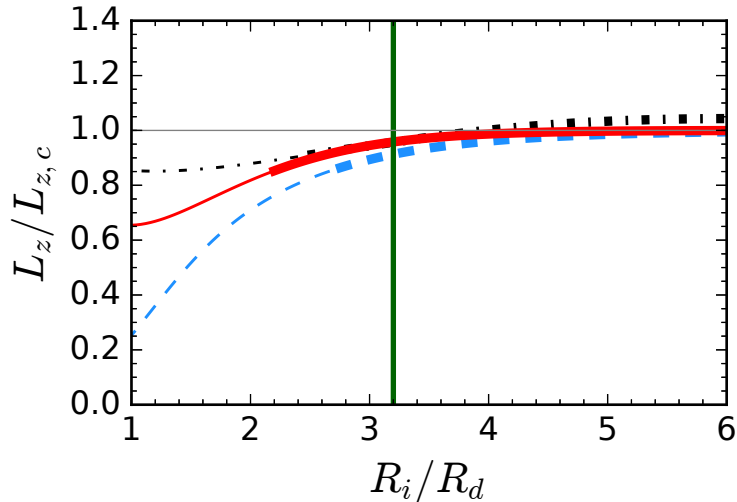


**Figure 3.** Radial distribution of orbital angular momentum for the following three disc models: Model  $\Sigma$  (blue, dashed), Model W (black, dot-dashed), and Model Q (red, solid), where  $R_d = 2.5$  kpc. The angular momentum content of each annulus is normalised by the angular momentum in the same annulus for an exponential disc that is entirely composed of stars in circular orbits ( $L_z(R_i)/L_{z,c}(R_i)$ ). Each annulus has width  $\delta R = 0.1$  kpc (sufficiently narrow that the curves appear continuous). A vertical, green line indicates the radius of normalisation ( $R_0 = 8$  kpc) for the appropriate surface density and radial velocity dispersion profiles described in §2.2. Thin lines indicate where each model has radial velocity dispersion  $\sigma_R > 50$  km s $^{-1}$ .

It follows that the normalised orbital angular momentum distribution for each model decreases toward the inner regions as the velocity dispersion increases.

The differences between the shapes of the curves for each orbital angular momentum profile in Figure 3 can be understood in terms of the differences in each model’s radial velocity dispersion profile and radial surface density profile. For the two models (Model  $\Sigma$  and Model Q) that adopt a Gaussian velocity distribution ( $P_G(\mathbf{v})_x$ ), the mean angular momentum profile is approximated by  $\langle L_z(R) \rangle \sim R \Sigma(R) (v_c - v_a(R))$ , where  $v_a \propto \sigma_R^2$ . By construction, these two models also have an exponential surface density profile (equation 6). Both of these models also have a radial velocity dispersion profile ( $\sigma_R(R)$ ) that goes to zero at large radii, and thus each normalised orbital angular momentum profile converges to unity with increasing radius. We also assume an exponential form for the normalisation of the surface density profile for Model W though this is not strictly self-consistent. An analysis of the robustness of approximating the integral of  $f_D$  over velocity space,  $\Sigma_D(R)$ , as an exponential with scale length  $R_d$  is given by Dehnen (1999). We note that at radii  $R_i/R_d \gtrsim 4$ , the surface density profile for  $\Sigma_D(R)$  has values greater than those of the exponential surface density profile used in the normalisation and those of models that adopt a Gaussian velocity distribution; this is consistent with the fact that the normalised orbital angular momentum profile for Model W has values greater than unity at  $R_i/R_d \gtrsim 4$ .

### 3 THE FRACTION OF STARS IN TRAPPED ORBITS

In order to investigate how stellar kinematics affect the fraction of a population that is in trapped orbits (hereafter denoted by  $\mathcal{F}$ ), we apply the capture criterion (equation A6) to our models of disc populations. In the method described below, we solve numerically for the fraction of stars in trapped orbits given a particular disc potential and form for the distribution function. We adopt the unperturbed, axisymmetric stellar distribution function, then impose a given spiral perturbation and evaluate for given value of the phase space coordinates whether or not the capture criterion (equation A6) is met. As we will see, stars with phase space coordinates not coincident with the corotation resonance can still be trapped, and the use of the unperturbed axisymmetric distribution in the calculation of the trapped fraction needs to be checked. Bovy (2015) investigated the response of both cold and warm 2D discs to a non-axisymmetric perturbation and found that the warmer the disc, the less it responded. Azimuthal (their tangential) velocity is the most important phase space coordinate in our analysis (our proxy for orbital angular momentum) and this is less affected than is the radial velocity. Bovy found that for typical weak non-axisymmetric perturbations, such as an elliptical disc or bar (the latter grown either adiabatically or rapidly), the mean tangential velocity at a given location is perturbed by less than 5%, in a disc with initial ratio  $\sigma_R/v_c < 0.2$  (see his Figures 26, 29 and 30). The amplitude of the response was seen to increase approximately linearly with the amplitude of the imposed potential. We expect that while our results will systematically over-predict the fraction of stars in trapped orbits, the trends we find with velocity dispersion and location will be valid.



The first step in the evaluation of the trapped fraction is to find the fraction of stars within each annulus,  $R_i + \delta R$ , that satisfies the capture criterion. The numerical integration for a given annulus is carried out assuming that the fraction is constant across the width of the annulus, and only one value of the radial coordinate is used, which corresponds to the inner radius of the annulus<sup>6</sup>.

We integrate the distribution function at  $R$  over the remaining phase-space – azimuthal coordinates,  $\phi$ , and velocity space coordinates,  $v_R$  and  $v_\phi$ , – with limits of integration set by the region of phase-space that satisfies the capture criterion. We set absolute limits of integration in velocity space  $\langle v_i \rangle \pm 100 \text{ km s}^{-1}$ , where  $i$  represents the radial or azimuthal components of the velocity vector. The solution to this integral, divided by the integral of the distribution function over all phase-space at  $R$ , is the fraction of stars in trapped orbits within a given annulus. We calculate the fraction of stars in trapped orbits for all annuli within  $R = R_{CR} \pm 4 \text{ kpc}$  for each choice of initial conditions. We thus find the radial distribution for the fraction of stars in trapped orbits per annulus,  $\mathcal{F}_R \equiv \mathcal{F}(R)$ , where the subscript “ $R$ ” indicates evaluation at the radial position  $R$  associated with that annulus.

We perform all integrations using the *Wolfram Mathematica v.8.0.4.0* software function `NIntegrate` with the parameters `AccuracyGoal` set to 8 significant digits and `MinRecursion` set to 8. We chose the values of these parameters to ensure convergence to a solution within a reasonable amount of time.<sup>7</sup> We set the bounds of integration to be the region of phase-space that satisfies the capture criterion using the `Boole` function.

Our primary focus here is to understand trends in the the relationship between the fraction of stars initially in trapped orbits and the stellar velocity dispersion ( $\sigma$ ) for the population and so the *relative trapped fraction between different models is of most interest*. In the process we explore how the fraction of stars in trapped orbits within a chosen radial range,

$$\mathcal{F}_{\Delta R} \equiv \int_{\Delta R} \mathcal{F}(R) dR, \quad (15)$$

depends on the adopted functional form of the distribution function and the parameter values of the spiral potential.<sup>8</sup> The subscript “ $\Delta R$ ” indicates that the fraction of stars in trapped orbits is evaluated by integrating over a specific radial range,  $\Delta R$ , of annuli, where the value for  $\mathcal{F}_i$  within each annulus has been evaluated over the non-axisymmetric azimuthal distribution of stars in trapped orbits (as described above). We henceforth refer to the fraction of stars in trapped orbits within a chosen radial range ( $\mathcal{F}_{\Delta R}$ ) as the “integrated fraction”. We do not evaluate the time evolution of the integrated fraction, and therefore refer to the fraction of stars that meets the capture criterion for a given model as the “initial” fraction. In §5.1, we argue that the initial fraction over-predicts the fraction of stars that could migrate radially.

For the entirety of this section we adopt either a radially fixed velocity dispersion profile and Gaussian distribution function ( $f_G(\mathbf{x}, \mathbf{v})$ ) or our simplest fiducial model, Model  $\Sigma$ . In Section 4, we use insights gained from these explorations to investigate the full fiducial models, Models  $\Sigma$ ,  $Q$ , and  $W$ , of the galactic disc.

### 3.1 Integrated Fraction for a Fixed Radial Velocity Dispersion and Gaussian Distribution Function

The fraction of stars in a given disc population that meets the capture criterion at a given spatial coordinate depends on the population’s velocity dispersion<sup>9</sup>. In this subsection we use a simple model to gain physical insight into the form of this dependence. We adopt the Gaussian phase space distribution function  $f_G(\mathbf{x}, \mathbf{v})$  (equation 10, described in §2.2.1), a radial velocity dispersion ( $\sigma_R$ ) that is constant within the disc and a fixed ratio between the radial and azimuthal velocity dispersions,  $\sigma_\phi/\sigma_R$ . The disc and spiral pattern are assumed to have the parameter values given in Table 1, with  $R_{CR} = 8 \text{ kpc}$ .

#### 3.1.1 Radial distribution of the fraction of stars in trapped orbits

Figure 4 shows the fraction of stars in trapped orbits at a range of radial coordinates for a given radial velocity dispersion,  $\sigma_R$ , ranging between 5 – 80  $\text{km s}^{-1}$ , in 5  $\text{km s}^{-1}$  increments. We devote the rest of this subsection to identifying the physics that determines the shapes of these curves. The intuition developed will be useful when we investigate more complex models later in this paper.

In the limiting case that  $\sigma_R \rightarrow 0$  and all orbits approach circular (in an axisymmetric potential), the radial distribution of the fraction of stars in trapped orbits saturates at 100% within the capture region and goes to zero at coordinates outside the capture region. An approximation for the integrated fraction ( $\mathcal{F}_{\Delta R}$ ) in this limit can be obtained from the ratio of the

<sup>6</sup> We validated this assumption provided the width is less than a typical epicyclic excursion.

<sup>7</sup> This is on order of a half hour of computing time per set of initial conditions with a 4 GHz processor.

<sup>8</sup> Equation 15 implicitly includes an integration of the chosen distribution function over all phase-space, excepting radial position, as described at the beginning of §3.

<sup>9</sup> This statement should not be confused with the fact that whether or not an *individual* disc star is in a trapped orbit is largely independent of its random orbital energy and determined primarily by its orbital angular momentum (or circular frequency)(Daniel & Wyse 2015).

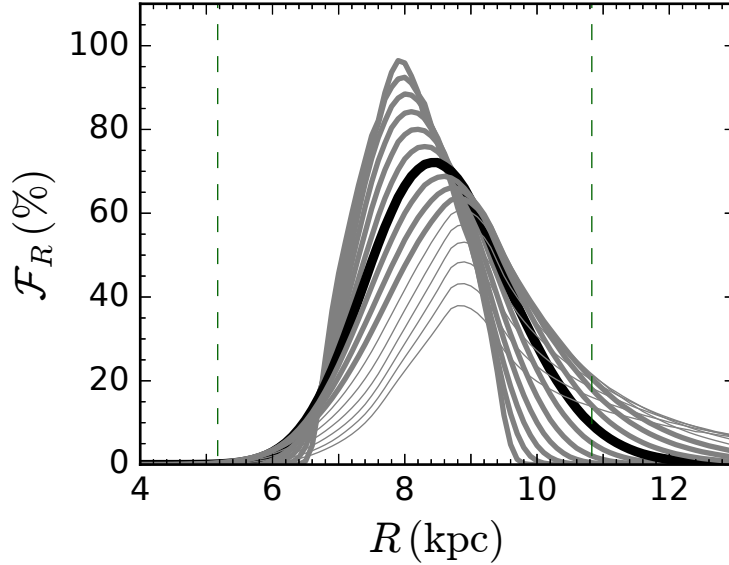


**Figure 4.** Radial distributions for the fraction of stars in trapped orbits, evaluated using the method described in the introduction of §3 and assuming a radially invariant radial velocity dispersion profile. The Gaussian form of the velocity distribution function ( $f_G$ ) has been adopted and the perturbing spiral potential has  $R_{CR} = 8$  kpc and parameter values given by Table 1. The assumed value of the radial velocity dispersion ranges from  $5 \text{ km s}^{-1}$  to  $80 \text{ km s}^{-1}$  in  $5 \text{ km s}^{-1}$  increments. For reference, the curve for the model that assumes  $\sigma_R = 35 \text{ km s}^{-1}$  is in bold. Thin lines indicate results for radial velocity dispersion  $\sigma_R > 50 \text{ km s}^{-1}$ . For reference, the thin, vertical, long-dashed (dark green) lines mark the inner and outer Lindblad resonances.

area of the capture region,  $A_{cap}$ , to the area of the annulus,  $A_{ann}$ , that spans the maximum radial range of the capture region. For low-amplitude spiral arms ( $\epsilon_\Sigma \lesssim 0.3$ ) that have a low pitch angle ( $\theta \lesssim 25^\circ$ ) the capture region follows closely the closed contours around the maxima in the effective potential (as seen in Figure 1(b)) and these in turn are well approximated by a sinusoidal function in the azimuthal direction (see equation 2). Under these conditions the area of the capture region may be evaluated as:

$$A_{cap} = \int_0^{2\pi} \int_{R_{CR} - (R_{CR} - R_{min})|\cos\phi|}^{R_{CR} + (R_{max} - R_{CR})|\cos\phi|} R dR d\phi, \quad (16)$$

where  $R_{min}$  and  $R_{max}$  denote the minimum and maximum radial coordinates of the capture region. Making the reasonable assumption that the capture region is symmetric around corotation, and being careful to note that the limits of integration involve  $|\cos\phi|$ , it is straightforward to show that  $A_{cap} = 4R_{CR}(R_{max} - R_{min})$ . The area of the annulus enclosing the capture region ( $A_{ann}$ ) is  $A_{ann} = 2\pi R_{CR}(R_{max} - R_{min})$ . The integrated fraction of stars in the annulus containing the capture region is therefore  $\mathcal{F}_{\Delta R} = 2/\pi \approx 64\%$ . Values higher than  $2/\pi$  can be obtained if the annulus over which the trapped fraction is integrated is narrower than the capture region, with the integration fraction approaching 100% around corotation, where the capture region spans all azimuthal coordinates. These limiting cases will be used to inform our interpretation of results that appear later in this paper.

The rms maximum radial excursion from the guiding centre radius, due to epicyclic motion, for a population with radial velocity dispersion  $\sigma_R$  is given by

$$X(R) = \frac{\sigma_R(R)}{\sqrt{2}\kappa(R)} \quad (17)$$

Thus in a disc with constant radial velocity dispersion and a flat rotation curve, the rms maximum radial epicyclic excursions scale as  $X \propto R$ . This typical maximum epicyclic excursion is a measure of how far from the limit of the capture region a star can be physically and still have its guiding centre within the capture region and be in a trapped orbit.

The curve in Figure 4 for the lowest velocity dispersion ( $\sigma_R = 5 \text{ km s}^{-1}$ ) peaks close to the corotation radius (8 kpc), and the fraction of stars in trapped orbits in annuli away from corotation approximately equals the fraction of azimuthal coordinates that are within the capture region. Populations of stars with higher values of their velocity dispersion, on more eccentric orbits, have a greater range of radial positions outside the capture region and therefore the distribution of stars in trapped orbits spreads over a greater radial range as seen in Figure 4. High velocity dispersion populations can have a distribution of stars in trapped orbits that extends beyond the inner and outer Lindblad resonances (radii at which  $\kappa = \pm m(\Omega_p - \Omega_c)$  – marked with long-dashed in Figure 4) where stars are likely to be scattered out of trapped orbits.

The location of the peak in the trapped fraction also depends on velocity dispersion, shifting to larger galactocentric radii

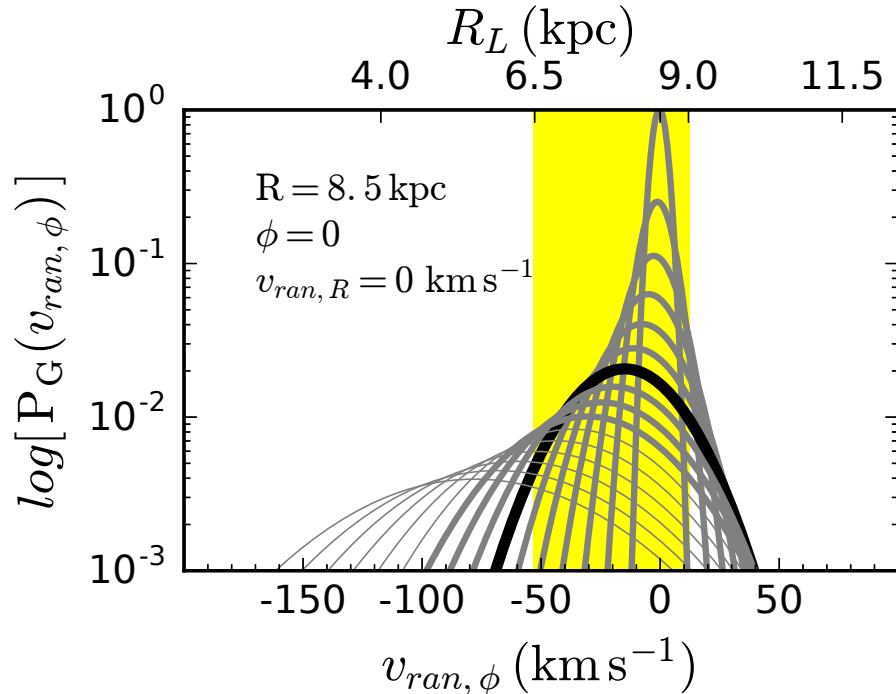


**Figure 5.** Distributions of the random azimuthal velocity ( $v_{ran,\phi}$ ) for stars observed at  $R = 8.5$  kpc, and  $\phi = 0$  (between the spiral arms, just beyond corotation at  $R_{CR} = 8$  kpc) with  $v_{ran,R} = 0$  km s $^{-1}$ . The underlying model is as Figure 4. The vertical axis shows the probability  $P_G(\mathbf{v})_{\mathbf{x}}$  on a logarithmic scale. Each curve represents a stellar population with a radial velocity dispersion ( $\sigma_R$ ) in the range  $5 - 80$  km s $^{-1}$ , in  $5$  km s $^{-1}$  increments. The thick (black) curve is for radial velocity dispersion  $\sigma_R = 35$  km s $^{-1}$ . The shaded (yellow) area indicates the range of azimuthal velocities that meet the capture criterion. The upper horizontal axis shows the guiding center radius ( $R_L$ ) associated with  $v_{ran,\phi}$ . Due to asymmetric drift, the peak in the random azimuthal velocity distribution shifts toward slower rotation with increasing velocity dispersion. In a corresponding manner, the peak of the probability distribution of guiding centre radii shifts toward radii that are closer to the galactic centre than the coordinate radius,  $R$ . Thin lines indicate model realisations that use radial velocity dispersion  $\sigma_R > 50$  km s $^{-1}$ .

for kinematically hotter populations. This reflects the shift in mean azimuthal velocity, represented by our simple asymmetric drift formula (equation 8). To understand this, first consider how the contribution to the integrated fraction from a stellar population at given coordinates  $\mathbf{x}$  depends on velocity dispersion. This is illustrated in Figure 5, which shows the distribution of random velocities in the azimuthal direction for stars observed at coordinates  $R = 8.5$  kpc,  $\phi = 0$  (just outside corotation, between the spiral arms), and with  $v_{ran,R} = 0$ . The different curves are for radial velocity dispersions in the range  $5 - 80$  km s $^{-1}$ , in  $5$  km s $^{-1}$  increments. The peak of the distribution of  $v_{ran,\phi}$  and of the corresponding distribution of guiding centre radii,  $R_L$ , shift to lower values with higher radial velocity dispersion. The yellow (shaded) region indicates those values of  $v_{ran,\phi}$  (and  $R_L$ ) that meet the capture criterion.

The radial coordinate of the peak in the radial distribution of the fraction of stars in trapped orbits ( $R_{peak}$  – in Figure 4) corresponds to the radius at which the mean guiding centre radius for the stellar population of interest equals the radius of corotation. The radius of corotation is the only radius at which all azimuthal coordinates are within the capture region, modulo a slight radial broadening for very strong spiral patterns (compare panels (b) and (c) in Figure 1). The mean guiding centre radius ( $\langle R_L \rangle$ ) of stars observed at coordinate  $R$  reflects the mean angular momentum of the stars, which in our prescription is set by the velocity dispersion, through the asymmetric drift equation (equation 8). Thus, stellar populations with velocity dispersion approaching zero ( $\sigma_R \rightarrow 0$ ), where the radial position of each star approaches its guiding centre radius ( $R \rightarrow R_L$ ), have  $R_{peak} \rightarrow R_{CR}$ .  $R_{peak}$  increases (moves to larger distances from the galactic centre) with increasing velocity dispersion. We show the dependence of  $R_{peak}$  on the radial velocity dispersion in Figure 6; the thick (black) curve represents the offset  $R_{peak} - R_{CR}$  for each value of the radial velocity dispersion shown in Figure 4.

These physical arguments suggest that the value of  $R_{peak}$  can be determined by finding the radius at which the mean guiding centre radius equals the radius of corotation. We then have:

$$\langle R_L \rangle = R \langle v_\phi \rangle / v_c$$

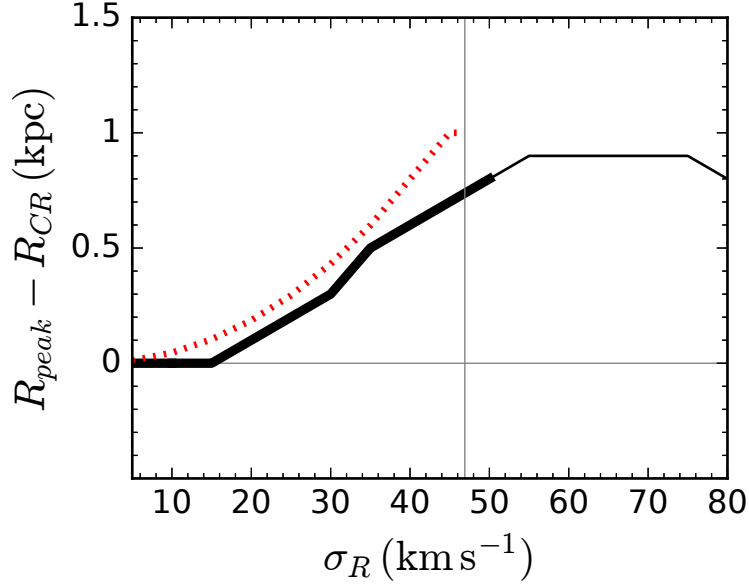


**Figure 6.** Radial offset of the location of the peak ( $R_{peak}$ ) in the distribution of the fraction of stars in trapped orbits ( $\mathcal{F}_R$ ) from the radius of corotation ( $R_{CR}$ ) as a function of the assumed fixed radial velocity dispersion ( $\sigma_R$ ). The solid (black) curve shows  $R_{peak} - R_{CR}$  calculated from the same models shown in Figure 4, while the dotted (red) curve shows the values predicted by equation 18 (with  $v_c = 220 \text{ km s}^{-1}$  and  $R_{CR} = 8 \text{ kpc}$ ), up to the critical velocity dispersion  $\sigma_{crit}$  from equation 19 beyond which this relation is invalid (indicated by the thin vertical line). Again, results for values of the radial velocity dispersion greater than  $50 \text{ km s}^{-1}$  are shown with thin lines. The increase in the shift of  $R_{peak}$  from  $R_{CR}$  as asymmetric drift increases with increasing values of the velocity dispersion is apparent.

so that

$$R_{peak} \langle v_\phi \rangle = R_{CR} v_c$$

and

$$R_{peak} - R_{CR} = R_{CR} \left( \frac{v_c}{v_c - v_a} - 1 \right). \quad (18)$$

The predicted relation from Equation 18 is shown in Figure 6 (dashed, red curve) together with the results from our models (solid, black curves). The relation from Equation 18 is a good match to the models, up to some critical value for the velocity dispersion, above which the offset  $R_{peak} - R_{CR}$  reaches a plateau. This maximum value for the offset is obtained when the radial coordinate for the population of stars that has a mean guiding centre radius equal to the radius of corotation is greater than, or equal to, the maximum radius of the capture region ( $R_{max}$ ). Beyond this limit, stars in the *peak* of the velocity distributions no longer meet the capture criterion and the contribution to the trapped fraction comes from stars in the broad, low-amplitude wings. Thus this critical value of the velocity dispersion marks the boundary above which the dominant contribution to the fraction of stars in trapped orbits changes from stars that have both radial positions and guiding centre radii inside the capture region to stars with guiding centre radii only inside the capture region. However since the capture region does not have constant radial width (see Figure 1), the transition between these two regimes is not abrupt.

An expression for this critical value of the radial velocity dispersion,  $\sigma_{crit}$ , may be obtained by considering the stellar population located at the maximum radius of the capture region and requiring that the mean angular momentum (per unit mass) of this population, given by  $\langle L_z \rangle = R_{max} \langle v_\phi \rangle$ , be equal to that of a star in a circular orbit at corotation (i.e.  $\langle L_z \rangle = R_{CR} v_c$ ). Given this requirement and our prescription for asymmetric drift (equation 8), the critical velocity dispersion may be expressed as:

$$\sigma_{crit} = \sqrt{C v_c \left( 1 - \frac{R_{CR}}{R_{max}} \right)} \quad (19)$$

The value of  $\sigma_{crit}$  for the parameter values of the model in Figure 6 is indicated by the thin, vertical line in that figure.

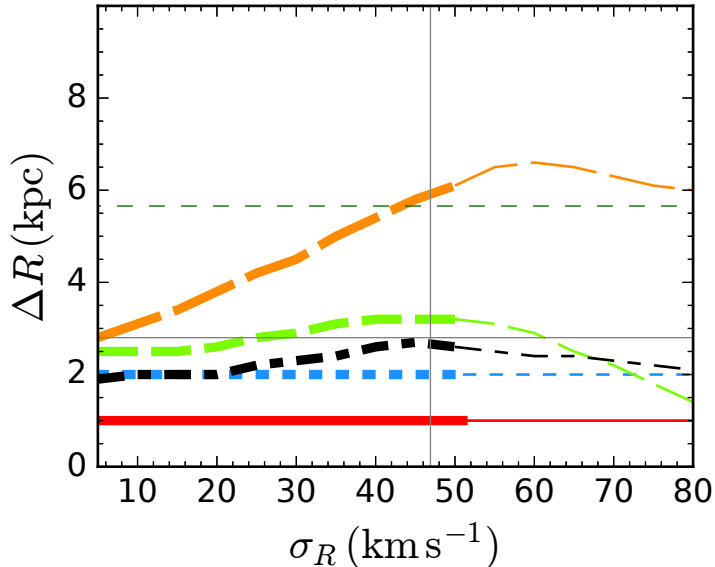


**Figure 7.** The width of the radial range ( $\Delta R$ ) used to evaluate the integrated fraction of stars ( $\mathcal{F}_{\Delta R}$ ) for  $R_{CR} \pm 0.5$  kpc ( $\Delta R_1$  – horizontal, solid, red),  $R_{CR} \pm 1$  kpc ( $\Delta R_2$  – horizontal, short-dashed, blue), and the radial range within which the annular fraction of stars in trapped orbits is  $> 5\%$  ( $\Delta R_{5\%}$  – long-dashed, orange),  $> 25\%$  ( $\Delta R_{25\%}$  – dashed, green), and greater than half the maximum value ( $\Delta R_{FWHM}$  – dot-dashed, black). Thinner segments of lines indicate radial velocity dispersion  $\sigma_R > 50$  km s $^{-1}$ . The measures of  $\Delta R$  shown here are evaluated for the same model illustrated in Figure 4. For reference, the thin, horizontal (dark-green) line indicates the distance between the inner and outer Lindblad resonances (dashed) and the horizontal grey line indicates the maximum width of the capture region. The thin, vertical line marks the critical velocity dispersion,  $\sigma_{crit}$ , from equation 19.

### 3.1.2 Definition of the radial range of evaluation

The fraction of stars initially in trapped orbits varies with radius and it is important to quantify how the integrated fraction ( $\mathcal{F}_{\Delta R}$ ) depends upon the radial range over which it is evaluated. We define this radial range,  $\Delta R$ , with two different approaches, the first a fixed physical width and the second depending on the shape of the distribution of the trapped fraction. Two of the measures of the trapped fraction, denoted  $\mathcal{F}_1$  and  $\mathcal{F}_2$ , are evaluated using annuli centred at the corotation radius and of fixed width  $\Delta R_1 = 1$  kpc and  $\Delta R_2 = 2$  kpc, respectively. We also evaluate three measures that do not have a fixed centre, rather these radial ranges for evaluation are defined in terms of the radial distribution of stars in trapped orbits. For these, denoted by  $\mathcal{F}_{5\%}$ ,  $\mathcal{F}_{25\%}$ , and  $\mathcal{F}_{FWHM}$ , the requirement is that in every annulus (each of width  $\delta R$ , given in Table 1) within the radial range of evaluation, the fraction of stars in trapped orbits must be greater than 5% (defining the radial range  $\Delta R_{5\%}$ ), 25% ( $\Delta R_{25\%}$ ), and half the maximum fraction captured ( $\Delta R_{FWHM}$ ), respectively.

The widths of the above radial ranges of interest are illustrated in Figure 7, for the model and parameter values of Figure 4. For low values of the velocity dispersion,  $R_{peak} \rightarrow R_{CR}$  and the shape-dependent radial ranges approach an annulus centred on corotation, as is prescribed for the fixed measures  $\Delta R_1$  and  $\Delta R_2$ . The variable widths generally are larger than the fixed widths, as seen in the figure. Radial ranges narrower than the capture region will give higher integrated fractions than wider radial ranges and indeed can lead to higher values than the  $\sim 64\%$  we estimated for widths equal to that of the capture region. Again, the widest radial ranges at high velocity dispersions can be comparable to the distance between the inner and outer Lindblad resonances in Figure 7 and may include stars that are likely to be scattered out of trapped orbits.

An illustration of these various measures of the radial range of integration is given in Figure 8, applied to the curve of the distribution of the trapped fraction for populations with  $\sigma_R = \{15, 35, 55\}$  km s $^{-1}$ , from Figure 4. For populations with high radial velocity dispersion (e.g.,  $\sigma_R = 55$  km s $^{-1}$  in Figure 8), the peak of the distribution of stars in trapped orbits may not be included in evaluations of the integrated fraction that use a fixed radial range ( $\Delta R_{1,2}$ ).

### 3.1.3 Dependence of the integrated fraction on velocity dispersion

Figure 9 shows the integrated fractions  $\mathcal{F}_1$ ,  $\mathcal{F}_2$ ,  $\mathcal{F}_{5\%}$ ,  $\mathcal{F}_{25\%}$ , and  $\mathcal{F}_{FWHM}$ , together with the best-fit linear fits to the trends as a function of velocity dispersion, for the model parameters of this subsection. The open symbols and thin lines denote values of the radial velocity dispersion above 50 km s $^{-1}$ , and the thin, vertical line indicates the critical velocity dispersion,  $\sigma_{crit}$ , above which one might expect a change in behaviour.

As seen in Figure 7, for velocity dispersions below around 30 km s $^{-1}$ , the radial ranges used to calculate the trapped

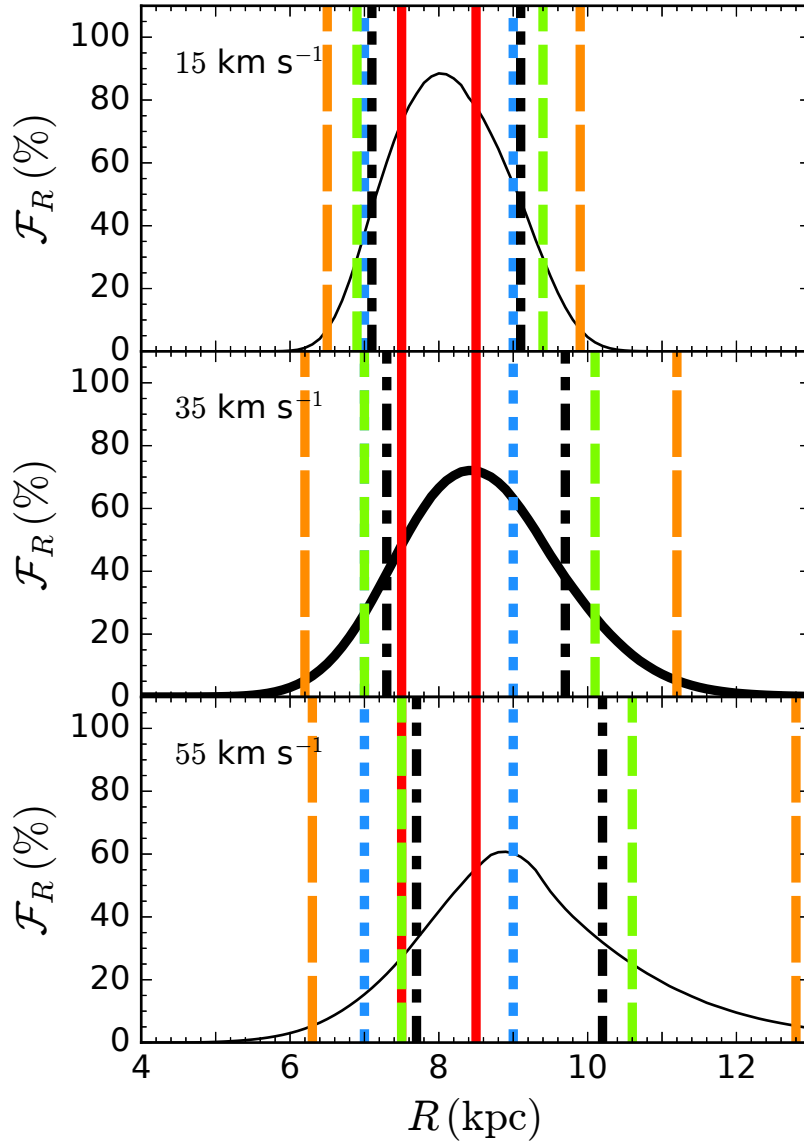


**Figure 8.** Illustration of the various measures of the radial range for integration of the trapped fraction, applied to the distribution of trapped fraction with radial velocity dispersions  $\sigma_R = \{15, 35, 55\}$   $\text{km s}^{-1}$  as indicated in each panel. The line types are taken from Figure 7.

fractions are narrower than the capture region, with the exception of  $R_{5\%}$ . This explains why the various measures of the trapped fraction are higher than the 64% that was derived earlier for the radial extent equal to the capture region. The values of the measure  $\mathcal{F}_{5\%}$  follows our expectations. This measure includes a larger fraction of the disc and should be more representative, modulo the caution that at large values of the velocity dispersion the radial range becomes so wide that interactions with the Lindblad resonances cannot be ignored. Indeed it is for this reason that we do not make an evaluation of the trapped fraction by integrating over the entire disc, but rather limit the evaluation to the maximum radial range provided by  $\Delta R_{5\%}$  and caution that  $\mathcal{F}_{5\%}$  may include a significant population that is scattered out of trapped orbits, particularly at high velocity dispersions.

All measures of the trapped fraction show a clear, approximately linear, decrease with increasing velocity dispersion of the stellar population. The linear<sup>10</sup> fits shown in the figure used the function `LinearModelFit` from *Wolfram Mathematica*'s built-in library<sup>11</sup> The values of the slope and zeropoint of the following linear fit are given in Table 3:

<sup>10</sup> We also explored exponential, polynomial, and Gaussian functional forms, but there is no compelling physical reason to include these more complex relationships.

<sup>11</sup> We set the fit "method" to "Automatic", thus allowing *Mathematica* to select from its library to minimize fitting residuals.

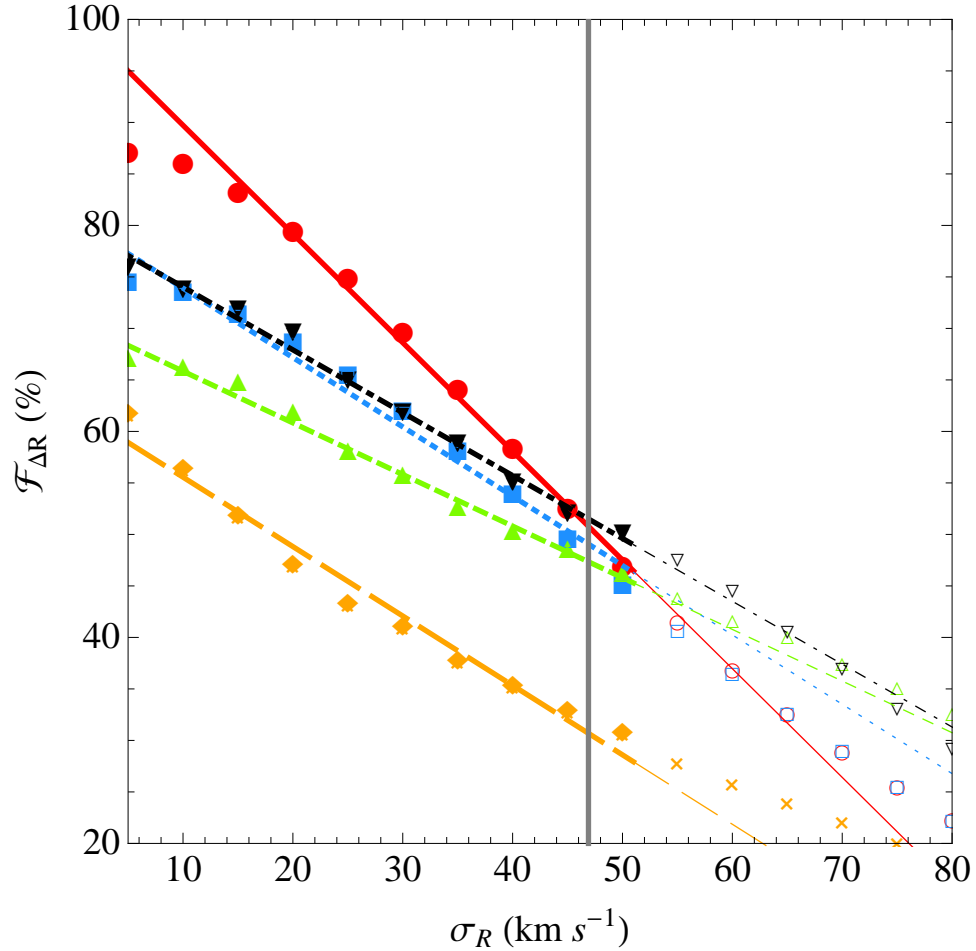


**Figure 9.** The evaluations for  $\mathcal{F}_1$ ,  $\mathcal{F}_2$ ,  $\mathcal{F}_{5\%}$ ,  $\mathcal{F}_{25\%}$ , and  $\mathcal{F}_{FWHM}$ , marked with circles (red), squares (blue), diamonds (orange), triangles (green), and downward-facing triangles (black), respectively. Best linear fits for  $\mathcal{F}_1$  (solid, red),  $\mathcal{F}_2$  (short-dashed, blue),  $\mathcal{F}_{5\%}$  (long-dashed, orange),  $\mathcal{F}_{25\%}$  (dashed, green), and  $\mathcal{F}_{FWHM}$  (dot-dashed, black). The fitting parameters for equation 20 are given in Table 3. The open symbols and thin lines indicate an assumed radial velocity dispersion  $\sigma_R > 50 \text{ km s}^{-1}$  and the vertical grey line indicates the critical value of the velocity dispersion from equation 19.

**Table 3.** The slopes and zero-points for the best-fit linear dependences of the integrated fractions of stars in trapped orbits as a function of radial velocity dispersions ( $5 \leq \sigma_R \leq 50 \text{ km s}^{-1}$ ). The underlying model parameter values are given in Table 1.

Integrated Fraction	Slope	$y$ -intercept
$\mathcal{F}_{\Delta R}$	$\xi_\mu$	$\xi_\beta$
$\mathcal{F}_1$	-1.1	100
$\mathcal{F}_2$	-0.7	81
$\mathcal{F}_{5\%}$	-0.7	62
$\mathcal{F}_{25\%}$	-0.5	71
$\mathcal{F}_{FWHM}$	-0.6	80

$$\mathcal{F}_{\Delta R}(\sigma_R) = \xi_\mu \sigma_R + \xi_\beta, \quad (20)$$

We expect the values of the fitting constants,  $\xi_\mu$  and  $\xi_\beta$ , to depend on the underlying parameters such as the radius of corotation and the amplitude of the spiral potential, and explore this in section §3.3.

### 3.2 Integrated Fraction for Radially Dependent Velocity Dispersion

Our assumption in the last section that the radial velocity dispersion is constant with radius is reasonable provided that only a relatively narrow range of radius is being considered. We now explore how the trends in the integrated fraction shown in §3.1 are modified when a radially dependent velocity dispersion profile ( $\sigma_R = \sigma_R(R)$ ) is assumed.

Throughout this subsection we assume Model  $\Sigma$ , which is summarized in Table 2 and uses the disc and spiral potentials described in §2.1 with parameter values given by Table 1, unless otherwise stated. This model assumes an exponential radial velocity dispersion profile, with scale length twice that of the assumed exponential disc. We explore a range of normalisations at corotation,  $\sigma_R(R = 8 \text{ kpc}) = \{5, 80\} \text{ km s}^{-1}$  in  $5 \text{ km s}^{-1}$  intervals. The dependence of the typical (rms) amplitude of epicyclic excursions (equation 17) on both epicyclic frequency ( $\kappa(R)$ , equation A3) and the local value for the radial velocity dispersion ( $\sigma_R(R)$ ) is taken into account in the evaluation of the trapped fraction.

The results are illustrated in Figure 10 where individual panels are analogues of Figures 4-9) and show (a) the radial distribution of the initial fraction of stars in trapped orbits,  $\mathcal{F}_R(R)$ ; (b) the distance between the peak of  $\mathcal{F}_R(R)$  and the radius of corotation ( $R_{peak} - R_{CR}$ ), as a function of velocity dispersion normalisation; (c) the various radial ranges ( $\Delta R$ ) within which the integrated fraction is evaluated, and (d) the integrated fraction ( $\mathcal{F}_{\Delta R}$ ).

The main difference between the curves for  $\mathcal{F}_R$  in Figure 10(a) and Figures 4 is a steeper decline at larger galactocentric radii in the case of the radially varying velocity dispersion, particularly for larger values of the normalisation at corotation (8 kpc). This reflects the fact that the local velocity dispersion in the outer disc is lower compared to the invariant case, so that the typical epicyclic excursions are lower, such that stars observed in the outer disc are less likely to have guiding centres within the capture region around corotation. The trapped fraction is low in these regions, far from corotation, so the differences are not large in terms of parameters such as the integrated fraction, Figure 10(d). The widths of the various radial ranges (panel (c)) are also narrower, compared to the case of constant velocity dispersion, again reflecting the narrower distributions in panel (a). Other than these minor quantitative differences, the qualitative results agree in showing a decline of trapped fraction with increasing velocity dispersion.

### 3.3 Other Functional Dependencies for the Integrated Fraction

In this section, we assume the same model used in §3.1, where we adopt a Gaussian velocity distribution at each coordinate ( $f_G$ , described in §2.2.1), radially fixed radial velocity dispersion profile ( $\sigma_R = 35 \text{ km s}^{-1}$ ), and exponential surface density profile ( $\Sigma(R)$ , equation 6). Unless explicitly stated, model parameter values are given in Table 1.

The integrated fraction of stars initially in trapped orbits ( $\mathcal{F}_{\Delta R}$ ) depends on the size and shape of the capture region, which depends on the spiral pattern speed ( $\Omega_p$ ) and the underlying potential of the disc and spiral ( $\Phi(R, \phi) = \Phi_0(R) + \Phi_1(R, \phi)$ ) (for a complete description see Daniel & Wyse 2015, equation 17 and corresponding text). For a given pattern speed, the integrated fraction increases with increasing amplitude of the perturbation to the potential due to the spiral pattern ( $|\Phi_s|_{CR}$ ), since the width of the capture region is larger for stronger spiral strengths (see Appendix A). In our model, the strength of the spiral perturbation (equation 3) is written in terms of the radius of corotation ( $R_{CR}$ ), spiral pitch angle ( $\theta$ ), number of spiral arms ( $m$ ), the assumed surface density profile ( $\Sigma(R)$ ), and the fractional surface density enhancement of the spiral potential ( $\epsilon_\Sigma$ ) (see §2.1). The model assumes a flat rotation curve of given circular velocity, so that ‘corotation radius’ is a proxy for ‘pattern speed’. Figure 11 shows how the maximum width of the capture region ( $R_{max} - R_{min}$ ) in our model varies with increasing fractional surface density of the spiral pattern ( $\epsilon_\Sigma$ ) for fixed corotation radius (left panel) and with increasing radius of corotation ( $R_{CR}$ ) for fixed fractional surface density (right panel).

The curve in the lefthand panel of Figure 11 is approximately a parabola, so that the (maximum) width of the capture region scales as  $\epsilon_\Sigma^{1/2}$ . For all other parameters fixed (as here),  $\epsilon_\Sigma$  is linearly proportional to the amplitude of the spiral potential (equation 3). Previous work (Sellwood & Binney 2002, their equation 12), established the expectation that the maximum radial range of a trapped orbit would scale as the square root of the strength of the imposed perturbation. The dependence seen in the figure then would imply that the width of the capture region scale as the maximum radial range of a trapped orbit. Since stars can be in trapped orbits while their physical coordinates lie outside the capture region, this correspondence is expected to be only approximate.

The non-monotonic behaviour seen in the righthand panel reflects how, assuming the same fractional surface density ( $\epsilon_\Sigma$ ), the radial range of the capture region does not scale as  $\sqrt{|\Phi_s|_{CR}}$  as one might naively expect.<sup>12</sup> Figure 1 illustrates how, with increasing spiral amplitude, not only does the radial range of the capture region broaden, but also its shape acquires a skew distortion from the simple sinusoidal model assumed in the derivation of  $\mathcal{F}_{\Delta R}(\sigma_R \rightarrow 0)$  in §3.1.1 (the shape is mathematically described by the solutions to equation 17 in Daniel & Wyse 2015). This skew becomes more prominent for higher amplitude

<sup>12</sup> Our prescription for the amplitude of the spiral pattern ( $\Phi_s(R)$ ) depends on the (exponential) surface density profile ( $\Sigma(R)$ ) and the wave number ( $k(R)$ , equation 4), so that the peak amplitude goes as  $|\Phi_s|_{CR} \propto R_{CR} e^{-R_{CR}/R_d}$  (see §2.1) with maximum strength when  $R_{CR} = R_d$ .



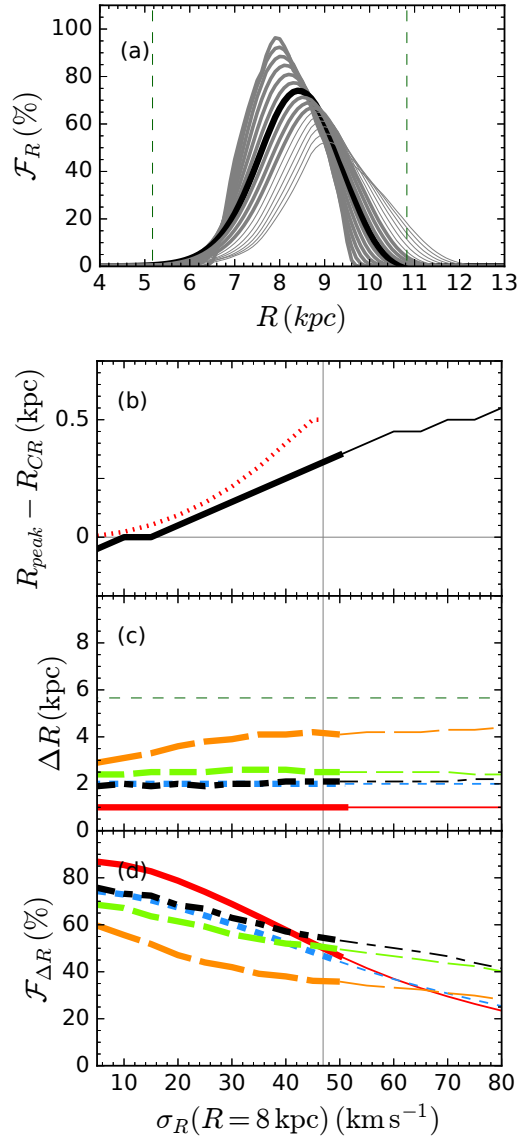


**Figure 10.** Dependence of the integrated fraction on the normalisation of the radial velocity dispersion profile in Model  $\Sigma$ , where  $\sigma_R \propto \Sigma(R)^{1/2} \propto e^{-R/R_\sigma}$  and the distribution function is given by  $f_G$ . The velocity dispersion is normalised at the radius of corotation such that  $\sigma_R(R=8 \text{ kpc}) = \{5, 80 \text{ km s}^{-1}\}$  in intervals of  $5 \text{ km s}^{-1}$ . Panels show (a) the radial distribution of the fraction of stars in trapped orbits ( $\mathcal{F}_R$ ), with the curve for  $\sigma_R(R=8 \text{ kpc}) = 35 \text{ km s}^{-1}$  in bold; (b) the distance between the peak of the radial trapped fraction profile and corotation ( $R_{\text{peak}} - R_{\text{CR}}$ ); (c) the radial range ( $\Delta R$ ) within which the integrated fraction is evaluated, and (d) the integrated fraction ( $\mathcal{F}_{\Delta R}$ ). Line styles have the same meaning as in Figs. 4-9. Thin lines and segments of lines in all panels indicate models that use a normalisation for the radial velocity dispersion  $\sigma_R(R=8 \text{ kpc}) > 50 \text{ km s}^{-1}$ . Thin, vertical, long-dashed (dark green) lines in panel (a) mark the inner and outer Lindblad resonances.

spiral perturbations. Thus for lower values of the corotation radius, where the surface density profile ( $\Sigma(R)$ , equation 6) is exponentially greater, the resulting radial range for the capture region is lower than the naive expectation, where the least skew distortion per spiral strength appears to occur at  $\sim 3R_d$  in our models.

We turn next to investigations of how the trapped fraction depends on these parameters of the model potential.

### 3.3.1 Integrated Fraction as a Function of Spiral Strength

We here use the value for the fractional surface density ( $\epsilon_\Sigma$ ) as a proxy for the amplitude of the spiral potential at corotation ( $|\Phi_s|_{\text{CR}}$ ) when all other parameters are held constant. In Figure 12, we use the same five values for the fractional surface density ( $\epsilon_\Sigma$ ) as in Figure 11 and a radially invariant radial velocity dispersion ( $\sigma_R = 35 \text{ km s}^{-1}$ ). Panel (d) of Figure 12 shows that the integrated fraction of stars in trapped orbits ( $\mathcal{F}_{\Delta R}$ ) increases smoothly with increasing fractional surface density

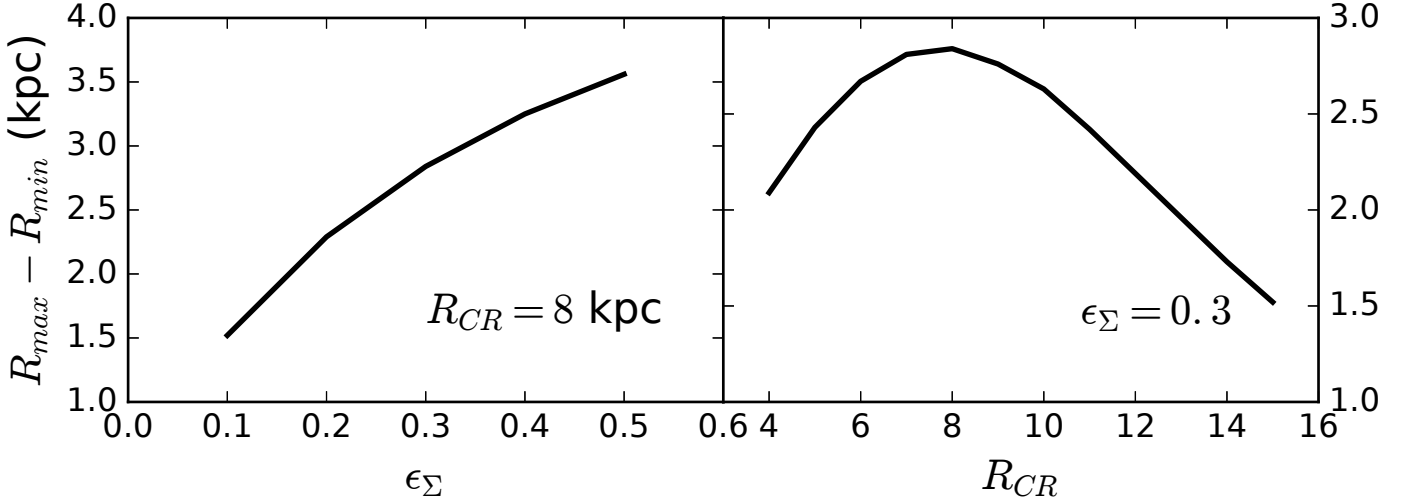


**Figure 11.** Both curves represent the maximum width of the capture region ( $R_{max} - R_{min}$ ). The panel on the left shows the maximum size of the capture region for  $\epsilon_{\Sigma} = \{0.1, 0.5\}$  in intervals of 0.1 and fixed radius of corotation ( $R_{CR} = 8$  kpc). The panel on the right shows the same measure for varying radius of corotation,  $R_{CR} = \{4, 15\}$  kpc in intervals of 1 kpc, and fixed  $\epsilon_{\Sigma} = 0.3$ .

( $\epsilon_{\Sigma}$ ). The shape of the curves in Figure 12(d) are remarkably similar to shape of the curve in the left hand side of Figure 11, indicating that the integrated fraction scales with the the maximum width of the capture region (or area, for given value of  $R_{CR}$ ). A similar behaviour is expected for the dependence of the integrated fraction on any other parameter that enters linearly in the expression for spiral strength (equation 3), such as number of arms ( $m$ ).

There is a 0.1 kpc decrease in the offset between corotation and the peak of the radial trapped fraction profile from  $\epsilon_{\Sigma} = 0.3$  to  $\epsilon_{\Sigma} = 0.4$ , as shown in panel (b) of Figure 12. This could arise from the relative importance of the skew in the shape of the capture region with increasing amplitude for the perturbing potential (see discussion in §3.3). However, it is difficult to draw significant conclusions about this shift since changes in the values for  $R_{peak} - R_{CR}$  between models are less than or on order of  $\delta R$  (Table 1).

There is a clear trend that the integrated fraction of stars in trapped orbits ( $\mathcal{F}_{\Delta R}$ ) increases with increasing spiral amplitude at corotation ( $|\Phi_s|_{CR}$ ). The fitting coefficients in equation 20 ( $\xi_{\mu, \beta}$ ) also depend on spiral strength, but we have found no simple scaling or transformation.

### 3.3.2 Integrated Trapped Fraction as a Function of Pattern Speed

In §3.3.1 we demonstrated that the integrated fraction of stars in trapped orbits ( $\mathcal{F}_{\Delta R}$ ) depends on the amplitude of the spiral perturbation to the potential at corotation ( $|\Phi_s|_{CR}$ ) since the maximum width of the capture region increases with increasing strength of the spiral perturbation. Our prescription for the amplitude of the spiral pattern, ( $\Phi_s(R)$ , equation 3) depends on the both the disc surface density profile, which we have chosen to be an exponential ( $\Sigma(R)$ , equation 6) and the wave number ( $k(R)$ , equation 4), such that the peak amplitude scales as  $|\Phi_s|_{CR} \propto R_{CR} e^{-R_{CR}/R_d}$  (see §2.1). In the introduction to this section (§3.3) and the right-hand panel of Figure 11 we showed that the maximum width of the capture region ( $R_{max} - R_{min}$ ) scales non-monotonically with the radius of corotation. In this subsection we explore how and why the integrated fraction depends on the radius of corotation ( $R_{CR}$ ), and its corresponding spiral pattern speed ( $\Omega_p = v_c/R_{CR}$ ), including the size of the capture region.

The size of epicyclic excursions, as well as the position and shape of the capture region, affect the radial distribution of stars in trapped orbits ( $\mathcal{F}_R$ ). In Figure 13, we set  $\sigma_R = 35$  km s $^{-1}$  at all radii, let the phase space distribution be given by  $f_G(\mathbf{x}, \mathbf{v})$  (§2.2.1), and calculate the various measures of trapped fraction ( $\mathcal{F}_R$ ) for pattern speeds corresponding to radii of corotation between 4 – 15 kpc, in 1 kpc intervals.

For fixed radial velocity dispersion ( $\sigma_R$ ) and flat rotation curve, the typical stellar radial epicyclic excursions increase linearly with galactocentric radius,  $X \propto R$  (see equation 17). The distribution of stars in trapped orbits ( $\mathcal{F}_R$ ) therefore depends on the radius of corotation ( $R_{CR}$ ) since both the maximum amplitude of epicyclic excursions ( $X$ ) and the width of the capture region ( $|R_{max} - R_{CR}| \approx |R_{CR} - R_{min}|$ ) set the maximum distance from corotation for stars in trapped orbits and  $R_{CR}$  sets the area of the capture region (see discussion following equation 17). The maximum range in radial coordinate for stars in trapped orbits is illustrated in panel (a) of Figure 13 and best quantified by  $\Delta R_{5\%}$  (long-dashed, orange) in panel (c).

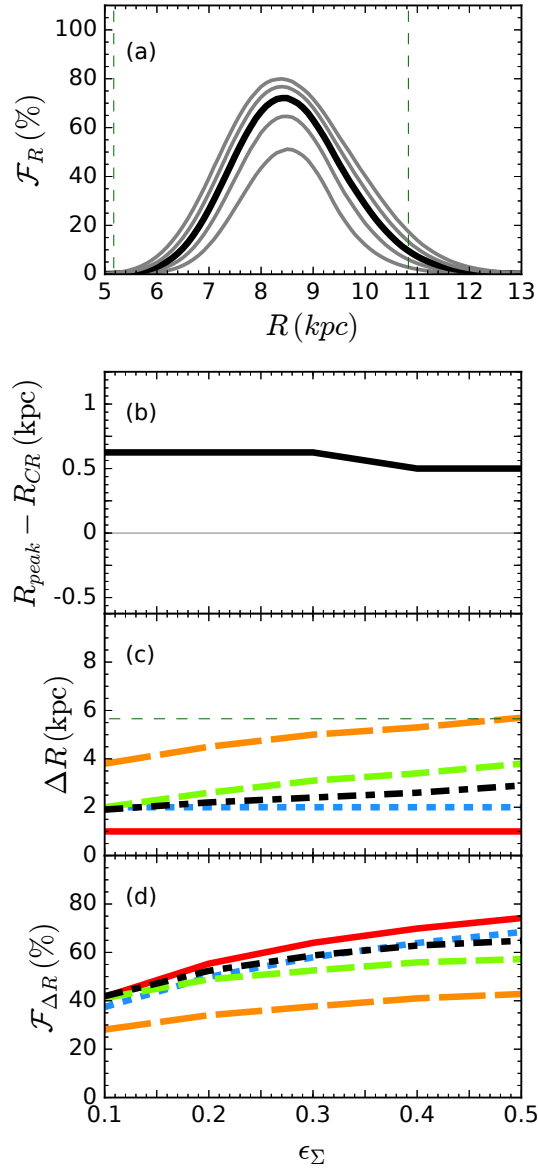


**Figure 12.** Dependence of the integrated fraction of stars in trapped orbits on the spiral strength,  $\epsilon_\Sigma$ , for  $\epsilon_\Sigma = 0.1 - 0.5$  in intervals of 0.1. Otherwise the underlying model assumptions are as in Figure 4, with  $\sigma_R = 35 \text{ km s}^{-1}$ . Panels show (a) the radial distribution of the fraction of stars in trapped orbits ( $\mathcal{F}_R$ ), with the bold curve indicating  $\epsilon_\Sigma = 0.3$ ; (b) the offset of the peak of the radial trapped fraction profile from corotation ( $R_{peak} - R_{CR}$ ); (c) the radial range ( $\Delta R$ ) within which the integrated fraction is evaluated, and (d) the integrated fractions of stars in trapped orbits ( $\mathcal{F}_{\Delta R}$ ). The line styles indicating the different definitions of the radial range for integration have the same meanings as in Figures 6-9.

The shape of the curve for  $\Delta R_{5\%}$  in Figure 13(c) is consistent with that for the width of the capture region as a function of corotation (see Figure 11) combined with the linear increase in typical maximum radial epicyclic excursions ( $X \propto R$ ).

Equation 18 predicts that the value for  $R_{peak} - R_{CR}$  scales as  $R_{CR}$  for fixed velocity dispersion (a consequence of epicyclic excursions scaling with radius in this regime). Panel (b) of Figure 13 illustrates this point. The curve in this plot is not smooth (and also in panel (b) of Figure 12). As stated in §3.3.1, this could be due to the relative importance of the skew in shape of the capture region with increasing spiral amplitude but it is unclear since changes in the values for  $R_{peak} - R_{CR}$  between models are less than or on order of  $\delta R$  (Table 1).

The trend is that the integrated fraction ( $\mathcal{F}_{\Delta R}$ ) generally decreases with increasing radius of corotation, equivalent to decreasing pattern speed. All evaluations of  $\mathcal{F}_{\Delta R}$  will naturally decrease in terms of the maximum value, since  $\mathcal{F}_R$  broadens with increasing  $R_{CR}$  (as also discussed in §3.1). Should the offset ( $R_{peak} - R_{CR}$ ) be large enough for the peak to be beyond the annulus over which the integrated fraction is evaluated, as can happen for fixed annular widths such as  $\Delta R_{1,2}$ , the integrated

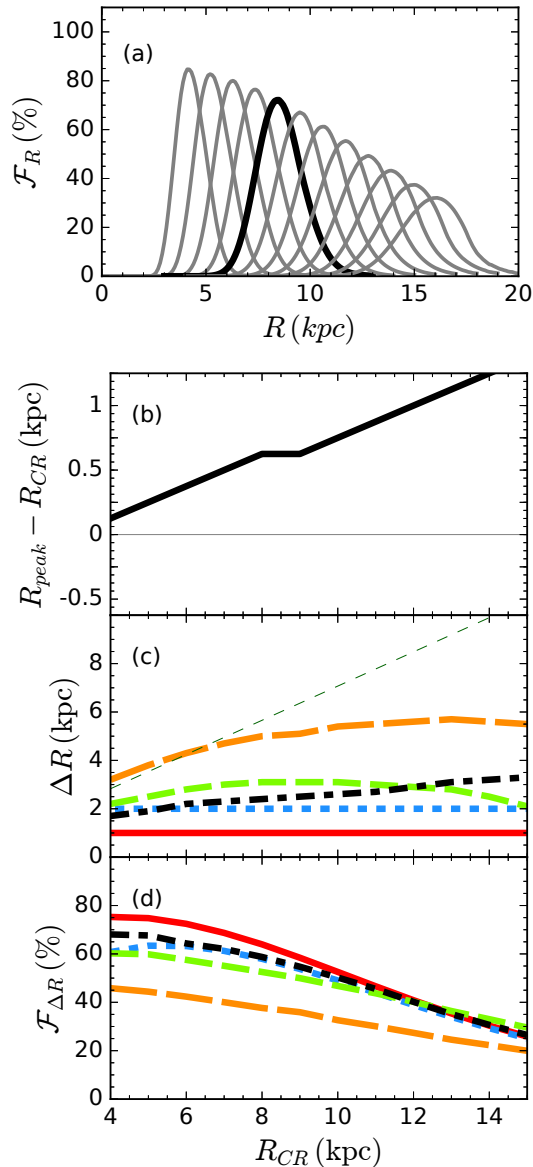


**Figure 13.** Dependence of the integrated fraction on the radius of corotation in the current adopted model, for  $R_{CR} = 4 - 15$  kpc in 1 kpc intervals. Remaining model assumptions are as in Figure 4 with  $\sigma_R = 35$  km s $^{-1}$ . Panels show (a) the radial distribution of the fraction of stars in trapped orbits ( $\mathcal{F}_R$ ), with the bold curve for  $R_{CR} = 8$  kpc; (b) the offset of the location of the peak value of the trapped fraction from corotation ( $R_{peak} - R_{CR}$ ); (c) the radial range ( $\Delta R$ ) within which the integrated fraction is evaluated, and (d) the integrated fraction of stars in trapped orbits ( $\mathcal{F}_{\Delta R}$ ). Line styles are the same as in Figures 6-9.

fraction in that case ( $\mathcal{F}_{\Delta R}$ ) decreases more rapidly with increasing corotation radius than when  $\mathcal{F}_{\Delta R}$  is evaluated using non-fixed radial ranges (i.e.  $\Delta R_{5\%,25\%,FWHM}$ ).

#### 4 INTEGRATED TRAPPED FRACTION IN MODELS OF THE GALACTIC DISC

In §3, we established that the value of the integrated fraction depends strongly on the value of the radial velocity dispersion at corotation ( $\sigma_R(R_{CR})$ ). We also found that the integrated fraction depends on the area and location of the capture region, the size of epicyclic excursions, and the spiral strength and pattern speed. These analyses in hand, we are equipped to interpret how our adopted forms for the stellar distribution function, including particular prescriptions for the radially dependent radial velocity dispersion profile, affect the derived behaviours of the integrated fraction over the disc.

Our results for the three fiducial models outlined in Table 2 are shown in Figure 14, for different values of the corotation radius such that  $R_{CR}$  varies between 4–15 kpc, in 1 kpc intervals. Each model adopts the parameter values in Table 1, where

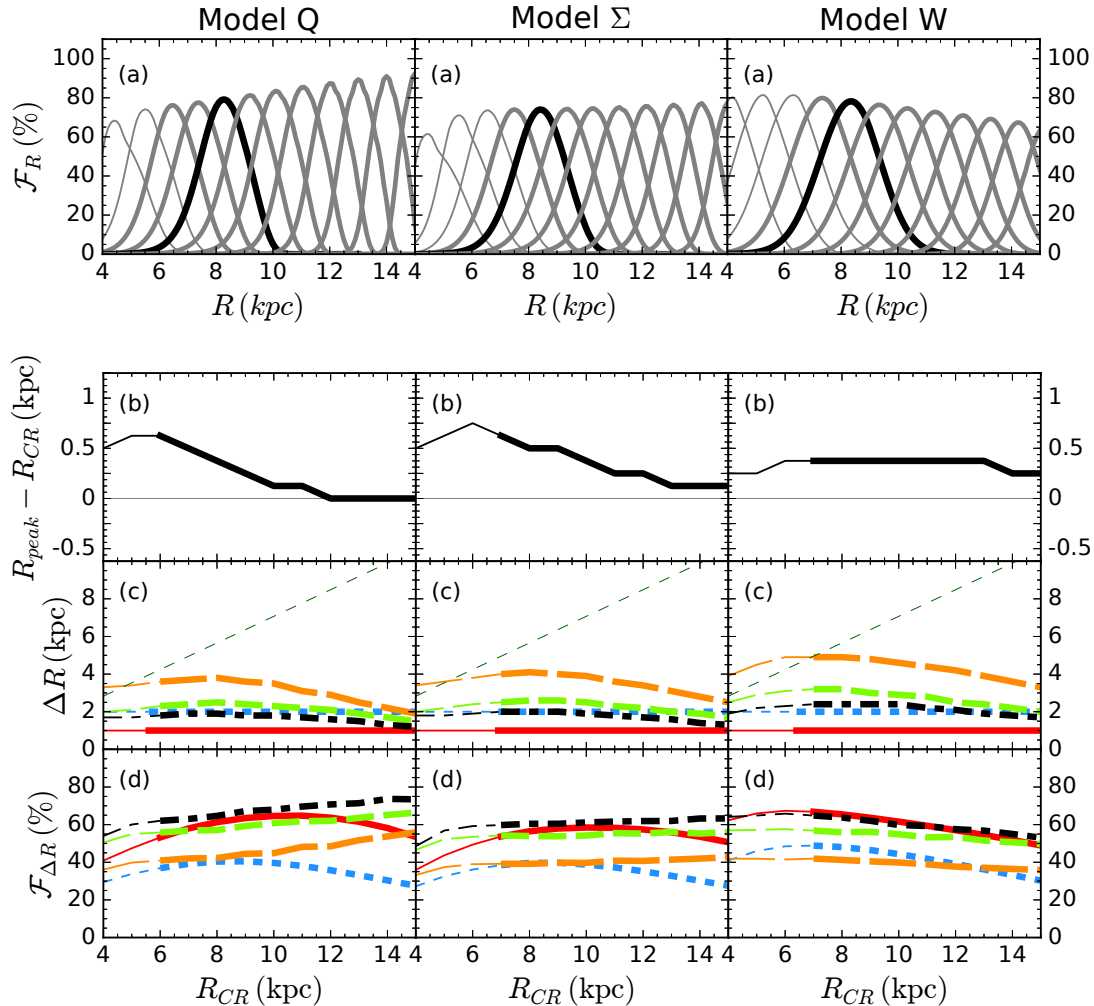


**Figure 14.** As Figure 13, the dependence of the integrated fraction on the radius of corotation, now for the three classes of model in Table 2. Each model assumes that the radial velocity dispersion profile is radially dependent, with a different form of the profile in each class of model. Panels show (a) the radial distribution of the fraction of stars in trapped orbits ( $\mathcal{F}_R$ ); (b) the offset of the location of the peak value of the trapped fraction from the radius of corotation ( $R_{peak} - R_{CR}$ ); (c) the radial range ( $\Delta R$ ) within which the integrated fraction is evaluated, and (d) the integrated ( $\mathcal{F}_{\Delta R}$ ). Line styles have the same meaning as in Figs. 4-9. Thin lines and line segments indicate that the value of the radial velocity dispersion at  $R_{CR}$  exceeds  $50 \text{ km s}^{-1}$ .

the normalisation of the radial velocity dispersion profile ( $\sigma_R(R)$ ) for each model is given in Table 2. In this section, we will only consider regions of the disc where  $\sigma_R \leq 50 \text{ km s}^{-1}$ .

For all values of the corotation radius, we find that the trends in the width of the unconstrained radial ranges for evaluation ( $\Delta R_{5\%}$ ,  $\Delta R_{25\%}$ , and  $\Delta R_{FWHM}$ ) and their corresponding integrated fractions ( $\mathcal{F}_{5\%}$ ,  $\mathcal{F}_{25\%}$ , and  $\mathcal{F}_{FWHM}$ ), primarily depend on both the area of the capture region and the typical amplitude of epicyclic excursions for stars in trapped orbits (parameterised by the rms maximum amplitude,  $X$ ). These in turn depend on the value of  $R_{CR}$ . The maximum radial width of the capture region, which closely scales in amplitude with its area, is shown as a function of corotation in the right hand panel of Figure 11. The width of the capture region depends on the adopted underlying potential (Daniel & Wyse 2015). The curve in the right hand panel of Figure 11 is applicable to all of our fiducial models and is consistent with the maximum radial width for the capture region roughly scaling with the radius of corotation as  $(R_{max} - R_{min}) \propto R_{CR} e^{-R_{CR}/3R_d}$ . The area of the capture region influences the radial width of the distribution of stars in trapped orbits and, more importantly, the local surface density or *number* of stars in trapped orbits. Taking into account that the shape and area of the capture region for a given radius of corotation is the same for all fiducial models (assuming fixed remaining parameters of the spiral) since they assume the same underlying potential, we can explore how the kinematics of each model affects the integrated fraction of stars in trapped orbits.

The radial dependence of the velocity dispersion affects the integrated fraction in two ways. First, the radial velocity dispersion sets the amplitude of radial epicyclic excursions,  $X \propto \sigma_R(R)/\kappa(R)$  (equation 17). In turn, the sizes of epicyclic

excursions affects the radial width of the distribution of stars in trapped orbits ( $\mathcal{F}_R$ ) since these determine the typical difference between a star's physical radial coordinate and that of its guiding centre. Second, the velocity dispersion sets the amplitude for the offset  $R_{peak} - R_{CR}$  (panels (b)) through its dependence on the asymmetric drift (see eqn 18 earlier). The behavior of the curves for each model in Figure 3, which illustrate how the velocity dispersion underlies the shape of the orbital angular momentum distribution, is related to this interdependence. The angular momenta decrease toward the galactic centre, compared to the case of all stars on circular orbits, as velocity dispersion increases. The overall consequence is that a lower fraction of stars near the galactic centre meets the capture criterion for each model. The values for unconstrained measures of the integrated fraction ( $\mathcal{F}_{\Delta R} = \mathcal{F}_{5\%,25\%,FWHM}$ ) quantify the shape of the distribution of stars in trapped orbits, where the range in radii for the various measures  $\mathcal{F}_R$  is closely approximated by that given by  $\Delta R_{5\%}$  (long-dashed, orange curve in panels (c)). The assumed radial velocity dispersion profile ( $\sigma_R(R)$ ) is therefore integral to understanding the integrated fraction  $\mathcal{F}_{\Delta R}$  for each model since it sets the radial dependence of the radial offset,  $R_{peak} - R_{CR}$ , and the shape (measured by  $\Delta R$ ) of the distribution of stars in trapped orbits. The following is a more detailed exploration of the distributions shown in Figure 14 for each model.

The radial velocity dispersion profile for Model W ( $\sigma_R(R) \propto e^{-R/3R_d}$ ) is relatively shallow (Figure 2, dot-dashed, black) and leads to an approximately constant value for  $R_{peak} - R_{CR}$  as the value for the corotation varies (Figure 14(b), last column). The curve for  $\Delta R_{5\%}$  peaks at approximately  $3R_d$  where its value is nearly 2 kpc greater than its minimum value. The shape of this curve arises from two competing effects. The first is the dependence of the area of the capture region on the value of  $R_{CR}$ , as described above and in the introduction to §3.3. Second, the amplitude of radial epicyclic excursions in Model W goes as  $X_W \propto R e^{-R/3R_d}$ . Thus, in Model W, the variation of the width of  $\mathcal{F}_R$  from epicyclic orbits equals the radial dependence for the total number of stars in trapped orbits and these two effects act in opposing fashions. The final result of this balance is that the value of the integrated fraction for  $\mathcal{F}_{5\%}$  (and other unconstrained measures of  $\mathcal{F}_{\Delta R}$ ) is nearly constant with radius. Fixed measures for  $\mathcal{F}_{\Delta R}$  (i.e.  $\mathcal{F}_{1,2}$ ) follow  $(R_{max} - R_{min})$  and do not have a significant radial dependence on asymmetric drift.

The radial velocity dispersion profile for Model Q approaches zero at large radii. Thus with increasing values for the corotation radius, the offset of the peak of the distribution of the trapped fraction ( $R_{peak} - R_{CR}$ ) goes to zero. Further, the unconstrained radial ranges converge to the width of the capture region (as most of the stars in trapped orbits are physically in the capture region), the maximum values for  $\mathcal{F}_R$  approach 100% (as most of the stars near corotation are in trapped orbits), and  $\mathcal{F}_{5\%}$  approaches  $\sim 64\%$  (the result from equation (16) in section 3.1.1 earlier). The amplitude of radial epicyclic excursions for Model Q goes as  $X_Q \propto R^2 e^{-R/R_d}$ , which peaks closer to the galactic centre (at  $2R_d$ ) than the expression for the radial range of the capture region at ( $\sim 3R_d$ ). Should the offset  $R_{peak} - R_{CR}$  be constant, this would have the effect of broadening the distribution of the trapped fraction compared to Model W. However, the offset  $R_{peak} - R_{CR}$  increases with decreasing corotation radii, reaching a value of nearly half the width of the capture region. The overall consequence is that a lower fraction of stars near the galactic centre meets the capture criterion, compared to Model W, and the integrated fraction for Model Q thus decreases toward the galactic centre.

The trends in the curves for Model  $\Sigma$  (Figure 14, middle column) are similar to those for Model Q. Both these models assume the same form for the distribution function ( $f_G$ ), but different radial velocity dispersion profiles. The normalisation for the radial velocity dispersion profile for Model  $\Sigma$  sets the local value for  $\sigma_R$  to greater values than in Model Q at all radii. Model  $\Sigma$  also has the steepest (declining with radius) radial velocity dispersion profile of all models and consequently has the lowest fraction of stars that meet the capture criterion toward the galactic centre (see also the dashed, blue curve in Figure 3). The radial velocity dispersion profile for Model Q was selected in order to approximate a disk that could support gravitational instabilities at all radii. Interestingly, this also produces a higher integrated fraction at all corotation radii.

For all models with radially dependent radial velocity dispersion profiles, the value for the integrated fraction ( $\mathcal{F}_{\Delta R}$ ) for any given radial range for evaluation ( $\Delta R$ ) is rather constant ( $\pm \sim 10\%$ ) as a function of corotation radius. This nearly constant value for the integrated fraction primarily arises from (1) the identical radial dependences for the radial range of the capture region (Figure 11) for each model and (2) the similar distribution of orbital angular momenta for stars with guiding centres within the capture region – where the associated measurables are the size of epicyclic excursions ( $X(R)$ ) and the offset  $R_{peak} - R_{CR}$  – due to the assumed kinematics for each model. As shown in §3.2, the integrated fraction decreases with increasing value for the normalisation of the velocity dispersion profile.

## 5 DISCUSSION

### 5.1 Integrated Trapped Fraction as an Upper Limit

The initial distribution of stars in trapped orbits derived above should be interpreted as an upper limit, for the following reasons. First, the parameter  $\Lambda_{nc,2}(t)$ , used to evaluate whether or not a star is in a trapped orbit, is explicitly a time-dependent quantity (equation A7) and we showed in Paper I that stars which initially satisfy the capture criterion could be

scattered<sup>13</sup> out of a trapped orbit before the torques from the spiral perturbation had time to change significantly that star's orbital angular momentum. Scattering events could affect the fraction of stars in trapped orbits over time (see discussion in Paper I, §3.3). This is an especially important point for stars in trapped orbits that either (1) have large radial excursions from the guiding centre, since such stars sample a larger fraction of the underlying disc potential and are therefore more likely to scatter as they encounter inhomogeneities in the disc,<sup>14</sup> or (2) meet a resonant criterion in addition to the corotation resonance – e.g. the path for the guiding centre radius crosses an ultra-harmonic Lindblad resonance.

Indeed, Barros et al. (2013) observed that a sufficiently long-lived spiral perturbation caused not only the pattern of angular momentum changes that correspond to trapped ‘horseshoe’ orbits, but also a later pattern of opposite angular momentum changes for stars close to the corotation radius, consistent with scattering processes.

Although it is generally accepted that discs are kinematically heated over time, the mechanisms and their relative importance aren't entirely clear. Carlberg & Sellwood (1985) argued that a rapidly growing spiral perturbation would cause a non-adiabatic response in the stellar disc over a broad radial range and a second order change in the orbital angular momentum distribution. In a high resolution follow up study using a pure stellar disk, Fujii et al. (2011) showed that even long lived material spiral arms kinematically heat the disk and they further supported this claim with analytic arguments. Indeed, Fujii et al. based their analytic argument for heating rates on those from GMCs and other small scale fluctuations in the galactic potential (Spitzer & Schwarzschild 1953; Wielen 1977; Lacey 1984). In any case, we have shown that a kinematically heated population of stars has a lower fraction of stars in trapped orbits. This implies that such heating by the spiral would over time lead to fewer stars being captured in trapped orbits than would be expected from the initial integrated fraction.

Our analysis assumes that all orbits are constrained to a 2D disc. This approximation is valid for stellar orbits that are nearly circular since the vertical and radial actions are separable (this is an underlying assumption in the derivation of the capture criterion, Daniel & Wyse 2015).<sup>15</sup> The vertical and radial actions may be coupled (and thus the validity of the capture criterion is untested) for a star that has large random motions. Further, the azimuthal force from the spiral (responsible for the changes in orbital angular momentum of a trapped star) will be weaker above/below the mid-plane. Our neglect of vertical motions thus overestimates how strongly stars in 3D orbits would interact with the spiral pattern. We therefore expect there is a systematic overestimate of the initial fraction of stars in trapped orbits with increasing velocity dispersion. As mentioned in §5.2, Solway et al. (2012) found an exponential decrease in the RMS change in orbital angular momentum for an ensemble of stars due to a transient spiral with increasing scale height of the population.

We defer a more thorough discussion of the time-dependence of the fraction of stars captured in trapped orbits to a later paper in this series (Paper IV).

## 5.2 Comparison to Previous Theoretical Work

A definition for maximum efficiency of radial migration from a single spiral pattern is the case in which the RMS change in orbital angular momentum for the ensemble of stars in trapped orbits,  $\langle(\Delta L_z)^2\rangle^{1/2}$ , is maximized over the spiral lifetime. This definition depends on the fraction of stars in trapped orbits (evaluated using  $\mathcal{F}_{\Delta R}$  in this paper), the amplitude of the change in *each* trapped star's angular momentum (maximum values can be estimated using the radial width of the capture region -  $R_{max} - R_{min}$ ), and the degree of scattering out of trapped orbits on timescales less than the timescale for radial migration.

Solway et al. (2012) used a simulation to study the relationship between  $\langle(\Delta L_z)^2\rangle^{1/2}$  for a population of stars and that population's scale height or initial radial velocity dispersion. They used seven tracer populations of test particles in a 3D disc with gravitational field defined by tapered, exponential thin and thick discs and two spiral arms. In two separate experiments each population was assigned either a different scale height or initial radial velocity dispersion. They found that the value for  $\langle(\Delta L_z)^2\rangle^{1/2}$  for a given stellar population decreases exponentially with linearly increasing values for the scale height. They also found that  $\langle(\Delta L_z)^2\rangle^{1/2}$  is smaller for populations with higher initial radial velocity dispersions.<sup>16</sup> It is encouraging that we also find a decline in the value for the integrated fraction of stars in trapped orbits,  $\mathcal{F}_{\Delta R}$ , with higher values for the radial velocity dispersion (§3.1.3), strengthening the argument that the efficiency of radial migration depends on the radial velocity dispersion.

It is not obvious how to further compare our results to the trend found by Solway et al. The value of  $\langle(\Delta L_z)^2\rangle^{1/2}$

<sup>13</sup> We define “scattering” as an event where a star's change in orbital angular momentum is correlated with a change in random orbital energy, distinct from radial migration.

<sup>14</sup> A star in a trapped orbit that has large excursions from its guiding centre could have a coordinate position that is distant from the capture region. In a realistic disc, such a trajectory would likely lead to scattering via interactions with inhomogeneities in the disc potential that are associated with objects such as dark matter substructure and giant molecular clouds. When modelling radial migration in the disc, one should also take care that the choice for  $\Delta R$  is less than the radial distance between spiral arms (here  $\lambda(R) = 2\pi/k(R)$ ), where the radial wavenumber  $k(R)$  (equation 4) is proportional to the number of spiral arms ( $m$ ).

<sup>15</sup> Indeed, we expect the capture criterion to be less robust for stars with highly non-circular orbits.

<sup>16</sup> Solway et al. (2012) do not find a functional form for the relationship between the RMS change in orbital angular momentum  $\langle(\Delta L_z)^2\rangle^{1/2}$  and initial radial velocity dispersion ( $\sigma_{r,0}$ ). However, we find that the closest fit to the data goes as  $\langle(\Delta L_z)^2\rangle^{1/2} \propto \sigma_{r,0}^{1/2}$ .

is, in general, a time dependent quantity (for example, due to the effects of scattering) for the entire population of stars. Solway et al. (2012) measured  $\langle(\Delta L_z)^2\rangle^{1/2}$  over the lifetime of the simulation in order to evaluate the final  $\langle(\Delta L_z)^2\rangle^{1/2}$  induced by a transient spiral pattern from initial growth through final decay. The integrated fraction ( $\mathcal{F}_{\Delta R}$ ) we have derived in this paper is a measure only of the initial fraction of stars that *may* migrate radially. We therefore interpret the fall off in the initial fraction of stars in trapped orbits with increasing velocity dispersion as a first step toward isolating the physics important to understanding the time-dependent value of  $\langle(\Delta L_z)^2\rangle^{1/2}$ . The time dependence for the fraction of stars in trapped orbits obviously depends on the rate of scattering. Nonetheless, it is expected that the effects of scattering will be less important for more open spiral arms (since even a star with large radial excursions from its guiding centre will not interact with the spiral away from corotation) and for perturbations with fewer spiral arms ( $m = 2$  rather than  $m = 4$  – since the Lindblad resonance will be farther from the radius of corotation).<sup>17</sup>

Further, we cannot make any predictions about whether or not the vertical position or motion of a star affects its trapped status because we have assumed a 2D disc on the premise that vertical action and radial action are separable (see Paper I, §2). Studies of simulated disc galaxies support the notion that the vertical velocity dispersion of a population negatively affects the degree to which it migrates radially (Vera-Ciro et al. 2014, 2016; Grand et al. 2016). However, should the ratio  $\sigma_R/\sigma_z$  be approximately constant, we expect a similar trend in the initial fraction of stars in trapped orbits as in equation 20.

Sellwood & Binney (2002, their equations 12) predict that the maximum change in angular momentum for a star that migrates radially,  $\Delta L_{max}$ , in a disc with a flat rotation curve is proportional to  $R|\Phi_s|_{CR}^{1/2}$ . Daniel & Wyse (2015) predict that the maximum possible change in orbital angular momentum for any individual star in a trapped orbit ( $\Delta L_{max}$ ) is set by the width of the capture region (Daniel & Wyse 2015, their §2.2.1). Figure 11 illustrates the dependence of the maximum width of the capture region ( $R_{max} - R_{min}$ ) on the fractional surface density for the spiral pattern ( $\epsilon_\Sigma$ ) and its radius of corotation ( $R_{CR}$ ). We expect that the maximum change in angular momentum per unit mass will be  $\Delta L_{max} \approx v_c(R_{max} - R_{min})$ . Whatever the functional form, the maximum possible change in angular momentum for a single star is of interest only in the sense that it is a limiting case, whereas the maximum amplitude for  $\langle(\Delta L_z)^2\rangle^{1/2}$  depends on the *distribution* of all the individual angular momenta of stars in trapped orbits. Indeed, Grand et al. (2016) find a positive correlation between the amplitude of a perturbation and the degree of induced radial migration in a suite of simulated disc galaxies.

Fouvry et al. (2015) predict that radial migration will be more important, for a given radial velocity dispersion  $\sigma_R$ , when the value for  $Q$  (equation 12) at corotation approaches unity since self-gravity strongly enhances perturbations to the potential at corotation. They develop a formalism which they use to compute a diffusion tensor in a razor thin disc and find that diffusion is parallel to the angular momentum axis at corotation, consistent with radial migration. In the series of models we use for Figure 13 we hold the radial velocity dispersion profile constant and vary the radius of corotation. The radial dependence for  $Q(R)$  would then be given by  $Q \propto (R e^{-R/R_d})^{-1}$  and would have a minimum value of  $Q \sim 0.7$  at  $R = R_d$ . Our models do not sample values of corotation inside  $R = 4$  kpc, but measures of the integrated fraction with unconstrained radial range of evaluation increase steadily toward the galactic centre. In Figure 13,  $Q = 1$  at  $R = 5.5$  kpc, corresponding to a more steep decrease in the values for the integrated fraction at  $R \gtrsim 5.5$  kpc. The comparison between Fouvry et al.’s results and ours is not direct. Fouvry et al. argue that a lower velocity dispersion leads to a stronger perturbation which stimulates more migration and we argue that a stronger perturbation traps more orbits, but the integrated fraction is lower for higher velocity dispersion. Additionally, our Model Q, which specifically sets the radial velocity dispersion so that  $Q = 1.5$  at all radii, has the lowest values for radial velocity dispersion profile at all radii (illustrated in Figure 2) and the highest values for the integrated fraction at all corotation radii. This is a somewhat obvious result and would presumably be more evident for lower values for  $Q$ .

Spiral patterns that corotate or nearly corotate with the disc can induce radial migration over large radial distances (Wada et al. 2011; Baba et al. 2013; D’Onghia et al. 2013; Grand et al. 2016, are examples of this phenomenon in N-body simulation). In Daniel & Wyse (2015) §4, we discuss how the radial range of the capture region depends on the radial rate of divergence between the spiral pattern speed and the circular orbital frequency for stars; this divergence rate equals zero for corotating spiral patterns and thus the capture region spans the full radial range of the spiral arm. The underlying assumptions for our models in this study have a divergence rate set by a flat rotation curve and radially constant pattern speed. We have not explored other divergence rates, but we expect the integrated fraction to decrease with increasing kinematic temperature in all cases since the underlying physics will be the same no matter the size of the capture region. A complication we have not addressed in this work is the consequence of overlapping resonances from multiple patterns (e.g., Minchev & Famaey 2010) or multiple transient modes (Sellwood & Carlberg 2014).

<sup>17</sup> Figure 7 and Table 3 from Solway et al. (2012) show that the value for  $\langle(\Delta L_z)^2\rangle^{1/2}$  is smaller for higher number of spiral arms, even when the prescription for the initial radial velocity dispersion is smaller for higher number of spiral arms (Table 1).



## 6 CONCLUSIONS

This is the second of a series of papers seeking to quantify the physical conditions under which radial migration is an important process in the evolution of disc galaxies. The efficiency of radial migration is directly related to the fraction of disc stars captured in trapped orbits, which is investigated here. We here apply the capture criterion we obtained in an earlier paper (a brief review is given in Appendix A of this work) to a series of models of a spiral galaxy (described in §2) in order to investigate how the adopted models and parameter values affect the initial distribution of the fraction of stars in trapped orbits ( $\mathcal{F}_R(R)$ ) and the integrated fraction ( $\mathcal{F}_{\Delta R}$ ) over one of several specified radial ranges ( $\Delta R$ ).

For any given spiral pattern,  $\mathcal{F}_R(R)$  depends on the distribution of orbital angular momentum near corotation ( $R_{CR}$ ) since whether or not a star is in a trapped orbit is well approximated by whether or not its guiding centre radius is within the capture region. At any given radial coordinate  $R$ , the velocity dispersion characterises the width of the azimuthal velocity distribution, and thus the distribution of orbital angular momentum at that radius. The capture criterion specifies the range of orbital angular momenta at a given spatial coordinate for a star to be in a trapped orbit. Therefore the fraction of a population that meets the capture criterion at radius  $R$  depends on the local velocity dispersion. We use the radial velocity dispersion as a proxy for the distribution of angular momentum since it is more easily observed and quantified. The profile for  $\mathcal{F}_R(R)$  for populations with high velocity dispersion has a radial range that is greater than the size of the capture region since the radial epicyclic excursions (parameterised by the maximum amplitude,  $X$ ) of these stars from their guiding centre radii ( $R_L$ , related to orbital angular momentum by equation A4) scales with the radial velocity dispersion (by equation 17). The peak of the distribution of the fraction of stars in trapped orbits has a smaller amplitude for populations with larger velocity dispersion. The offset of the peak of the distribution of stars in trapped orbits from the radius of corotation ( $R_{peak} - R_{CR}$ ) to larger radii is greater for populations with higher velocity dispersion (equation 18) due to the slower mean orbital velocity associated with asymmetric drift (§3.1.1).

The integrated fraction ( $\mathcal{F}_{\Delta R}$ ) is the measure we use to quantify how the fraction of stars in trapped orbits depends on the radial velocity dispersion. We evaluate  $\mathcal{F}_{\Delta R}$  by integrating the distribution of the trapped fraction over several specified radial ranges ( $\Delta R$ ), where we use two classification schemes for  $\Delta R$ . These are the radial ranges that have either fixed radial width centred around corotation ( $\Delta R_1$  and  $\Delta R_2$ ) or an unconstrained radial range ( $\Delta R_{5\%}$ ,  $\Delta R_{25\%}$ , and  $\Delta R_{FWHM}$ ) defined by the range within which the value for  $\mathcal{F}_R$  is greater than 5%, 25%, and half the maximum amplitude of the fraction of stars in trapped orbits as a function of radius. We use the combination of these fixed and unconstrained measures for  $\Delta R$  to gain the following insights into how the distribution of stars in trapped orbits depends on the adopted model and parameter values.

*The integrated fraction is smaller for stellar populations with higher velocity dispersion*, consistent with the trend found by Solway et al. (2012) (see §5.2). In Paper I, we analytically demonstrated that radial action, correlated with random orbital energy (i.e., the energy associated with non-circular motion), is mostly irrelevant to trapping. Indeed, it is the azimuthal action, or angular momentum in the epicyclic limit, that is primarily responsible for trapping. The kinematics of a *population* of stars at 2D coordinate  $\mathbf{x}$  can be described by the shape of a velocity ellipsoid having ratio  $\sigma_R/\sigma_\phi$ . The spread in the orbital angular momentum distribution (related to  $\sigma_\phi$  at  $R$  through the individual angular momenta given by  $L_z = R v_\phi$  per unit mass) is thus correlated with the radial velocity dispersion. In Figure 5, we illustrate how the spread in orbital angular momentum and asymmetric drift determine the fraction of stars in trapped orbits at coordinate  $\mathbf{x}$ . Figure 9 shows a linear fit (equation 20) for the integrated fraction (total fraction of stars in trapped orbits) as a function of radial velocity dispersion for each measure of  $\Delta R$  for the model that assumes constant  $\sigma_R$ . We argue that a similar trend exists for any reasonable distribution function since the decrease in the integrated fraction fundamentally stems from the broadening of the distribution of angular momentum.

The fitting constants are given in Table 3, where the maximum fraction of stars in trapped orbits over the radial range of the capture region ( $\mathcal{F}_{5\%}$  as  $\sigma_R \rightarrow 0$ ) is well approximated by  $\mathcal{F}_{\Delta 5\%, max} = 2/\pi \sim 64\%$  (§3.1.1). Further, we investigated the effect of using a radially dependent radial velocity dispersion profile (§3.2) and found that there are some differences in the distribution of stars in trapped orbits, but that the differences in the integrated fraction are not particularly significant as long as the radial velocity dispersion profile has a shallow radial gradient over the radial range of interest - as is the case for all models in this paper.

The distribution of stars (initially) in trapped orbits for populations with high velocity dispersion has a large radial range, spanning of order a few disc scale lengths. This is a consequence of the large radial excursions from the guiding centre radius for stars that meet the capture criterion (that the guiding centre radius lie within the capture region). However, the fraction of stars that meet the capture criterion at large radial distances from  $R_{CR}$  is small.

The maximum value for the integrated fraction  $\mathcal{F}_{\Delta R}$  over a given radial range ( $\Delta R$ ) is determined by the amplitude of the spiral perturbation at corotation.

The integrated fraction ( $\mathcal{F}_{\Delta R}$ ) for the fiducial Models  $\Sigma$ , Q, and W, is nearly independent ( $\pm \sim 10\%$ ) of corotation radius ( $R_{CR}$ ) or pattern speed ( $\Omega_p = v_c/R_{CR}$ ). Each model assumes an appropriate radially dependent radial velocity dispersion

profile ( $\sigma_R(R)$ ). The mean value for  $\mathcal{F}_{\Delta R}$  in these models depends on the normalisation of the radial velocity dispersion profile and the assumed amplitude for the spiral pattern.

The RMS change in orbital angular momentum,  $\langle(\Delta L_z)^2\rangle^{1/2}$ , around the radius of corotation of a spiral pattern depends on the fraction of stars in trapped orbits, which we have explored in this paper.  $\langle(\Delta L_z)^2\rangle^{1/2}$  also depends on the amplitude of the oscillations in orbital angular momentum for stars in trapped orbits (where the maximum amplitude oscillation for a guiding centre radius is given by the size of the capture region) and the time-scale for maximising  $\langle(\Delta L_z)^2\rangle^{1/2}$  due to these oscillations. Should the spiral disrupt on the time-scale for which each of these ingredients is maximal,  $\langle(\Delta L_z)^2\rangle^{1/2}$  would be maximised and radial migration would be most efficient for a single spiral. In §5.1, we argue that time dependent processes are an important part of understanding the efficiency of radial migration from a single spiral pattern, and thus  $\langle(\Delta L_z)^2\rangle^{1/2}$ , and the *initial* fraction of stars in trapped orbits should be treated as an upper limit. We defer exploration of the importance of scattering processes, the *distribution* of orbital angular momentum oscillation amplitudes, the *distribution* of time-scales for trapped orbits, and the consequences of a time-dependent spiral amplitude to later papers in this series.

## ACKNOWLEDGMENTS

It is a pleasure to thank J. Sellwood, R. Schönrich and P. McMillan for helpful discussions during the course of this study. We also thank the anonymous referee for thoughtful comments that have improved the quality of this work. This material is based upon work supported by the US National Science Foundation Graduate Research Fellowship under Grant No. DGE-1232825, National Science Foundation Grants AST-0908326 and OIA-1124403, and an American Association of University Women Dissertation Fellowship. RFGW thanks the Leverhulme Trust for a Visiting Professorship, held at the University of Edinburgh. She is also grateful for support from her sister, Katherine Barber. This work was performed in part at Aspen Center for Physics, which is supported by National Science Foundation grant PHY-1607611. RFGW thanks all at ACP for the wonderful environment for physics they have created and maintained.

## REFERENCES

- Baba J., Saitoh T. R., Wada K., 2013, *ApJ*, 763, 46  
 Barros D. A., Lépine J. R. D., Junqueira T. C., 2013, *MNRAS*, 435, 2299  
 Binney J., Tremaine S., 2008, *Galactic Dynamics: Second Edition*. Princeton University Press  
 Bovy J., 2015, *ApJS*, 216, 29  
 Bovy J., Rix H.-W., Liu C., Hogg D. W., Beers T. C., Lee Y. S., 2012, *ApJ*, 753, 148  
 Carlberg R. G., Sellwood J. A., 1985, *ApJ*, 292, 79  
 Contopoulos G., 1973, *ApJ*, 181, 657  
 Daniel K. J., Wyse R. F. G., 2015, *MNRAS*, 447, 3576  
 Daniel K. J., Wyse R. F. G., 2018, *MNRAS*, in preparation  
 Dehnen W., 1999, *AJ*, 118, 1201  
 Dehnen W., Binney J. J., 1998, *MNRAS*, 298, 387  
 D’Onghia E., Vogelsberger M., Hernquist L., 2013, *ApJ*, 766, 34  
 Fouvry J.-B., Binney J., Pichon C., 2015, *ApJ*, 806, 117  
 Freeman K. C., 1970, *ApJ*, 160, 811  
 Fujii M. S., Baba J., Saitoh T. R., Makino J., Kokubo E., Wada K., 2011, *ApJ*, 730, 109  
 Grand R. J. J., Springel V., Gómez F. A., Marinacci F., Pakmor R., Campbell D. J. R., Jenkins A., 2016, *MNRAS*, 459, 199  
 Hayden M. R., Bovy J., Holtzman J. A., Nidever D. L., Bird J. C., Weinberg D. H., Andrews B. H., Majewski S. R., et al., 2015, *ApJ*, 808, 132  
 Kordopatis G., Binney J., Gilmore G., Wyse R. F. G., Belokurov V., McMillan P. J., Hatfield P., Grebel E. K., et al., 2015, *MNRAS*, 447, 3526  
 Kuijken K., Gilmore G., 1991, *ApJL*, 367, L9  
 Lacey C. G., 1984, *MNRAS*, 208, 687  
 Lewis J. R., Freeman K. C., 1989, *AJ*, 97, 139  
 Lin C. C., Shu F. H., 1964, *ApJ*, 140, 646  
 Lin C. C., Yuan C., Shu F. H., 1969, *ApJ*, 155, 721  
 Loebman S. R., Debattista V. P., Nidever D. L., Hayden M. R., Holtzman J. A., Clarke A. J., Roškar R., Valluri M., 2016, *ApJL*, 818, L6  
 Loebman S. R., Roškar R., Debattista V. P., Ivezić Ž., Quinn T. R., Wadsley J., 2011, *ApJ*, 737, 8  
 Lynden-Bell D., Kalnajs A. J., 1972, *MNRAS*, 157, 1  
 Martinez-Medina L. A., Pichardo B., Peimbert A., Carigi L., 2017, *MNRAS*, 468, 3615

Minchev I., Famaey B., 2010, *ApJ*, 722, 112  
 Minchev I., Famaey B., Quillen A. C., Di Matteo P., Combes F., Vlahić M., Erwin P., Bland-Hawthorn J., 2012, *A&A*, 548, A126  
 Nordström B., Mayor M., Andersen J., Holmberg J., Pont F., Jørgensen B. R., Olsen E. H., Udry S., Mowlavi N., 2004, *A&A*, 418, 989  
 Pasetto S., Grebel E. K., Zwitter T., Chiosi C., Bertelli G., Bienayme O., Seabroke G., Bland-Hawthorn J., Boeche C., Gibson B. K., Gilmore G., Munari U., Navarro J. F., Parker Q., Reid W., Silvieo A., Steinmetz M., 2012, *A&A*, 547, A71  
 Peschken N., Athanassoula E., Rodionov S. A., 2017, *MNRAS*, 468, 994  
 Radburn-Smith D. J., Roškar R., Debattista V. P., Dalcanton J. J., Streich D., de Jong R. S., Vlahić M., Holwerda B. W., Purcell C. W., Dolphin A. E., Zucker D. B., 2012, *ApJ*, 753, 138  
 Roškar R., Debattista V. P., Loebman S. R., 2013, *MNRAS*, 433, 976  
 Roškar R., Debattista V. P., Quinn T. R., Stinson G. S., Wadsley J., 2008, *ApJL*, 684, L79  
 Schönrich R., Binney J., 2009, *MNRAS*, 399, 1145  
 Schönrich R., McMillan P. J., 2017, *MNRAS*, 467, 1154  
 Sellwood J. A., 2014, *Reviews of Modern Physics*, 86, 1  
 Sellwood J. A., Binney J. J., 2002, *MNRAS*, 336, 785  
 Sellwood J. A., Carlberg R. G., 2014, *ApJ*, 785, 137  
 Shu F. H., 1969, *ApJ*, 158, 505  
 Solway M., Sellwood J. A., Schönrich R., 2012, *MNRAS*, 422, 1363  
 Spitzer Jr. L., Schwarzschild M., 1953, *ApJ*, 118, 106  
 Toomre A., 1964, *ApJ*, 139, 1217  
 van der Kruit P. C., Searle L., 1981, *A&A*, 95, 105  
 Vera-Ciro C., D’Onghia E., Navarro J., Abadi M., 2014, *ApJ*, 794, 173  
 Vera-Ciro C., D’Onghia E., Navarro J. F., 2016, *ApJ*, 833, 42  
 Wada K., Baba J., Saitoh T. R., 2011, *ApJ*, 735, 1  
 Wielen R., 1977, *A&A*, 60, 263  
 Wielen R., Fuchs B., Dettbarn C., 1996, *A&A*, 314, 438

## APPENDIX A: THE CAPTURE CRITERION

In Paper I, we derived a “capture criterion” that can be used to determine whether or not a star in an infinitely thin (2D) disc is in a trapped orbit. As defined in §1, trapped orbits occur near the radius of corotation with a spiral pattern (or any density perturbation) and are characterised by having oscillatory orbital angular momentum with little to no change in random orbital energy (as also discussed in Sellwood & Binney (2002)). A star that is in a trapped orbit could migrate radially should the spiral pattern be transient. In this section we briefly review the capture criterion, but refer the reader to Paper I for a more complete derivation and discussion.

The capture criterion can be applied to any disc star given its 4D phase space coordinate  $(R, \phi, v_R, v_\phi)$ , the amplitude of the spiral perturbation to the potential at the radius of corotation,  $|\Phi_s|_{CR}$ , and the slope of the rotation curve at corotation (see Daniel & Wyse 2015, equation 32).

It is both informative and convenient to express the capture criterion in terms of orbital energy and orbital angular momentum. The orbital energy in the inertial frame ( $E$ ) and orbital angular momentum ( $L_z$ ) can be combined to form an expression for a conserved quantity known as the Jacobi integral (Binney & Tremaine 2008, eqns. 3.113),

$$E_J = E - \Omega_p L_z = \frac{1}{2} |\dot{\mathbf{x}}|^2 + \Phi_{eff}(\mathbf{x}), \quad (\text{A1})$$

with

$$\Phi_{eff}(\mathbf{x}) \equiv \Phi(\mathbf{x}) - \frac{1}{2} |\boldsymbol{\Omega}_p \times \mathbf{x}|^2 \quad (\text{A2})$$

being the effective potential (Binney & Tremaine 2008, eqns. 3.114), and  $\mathbf{x}$  and  $\dot{\mathbf{x}}$  being, respectively, the position and velocity of the star in the rotating frame. Since the spiral potential is time-independent in the rotating frame, it is in this frame that the Jacobi integral is conserved.

Figure A1 shows a Lindblad diagram for stars in a disc with a flat rotation curve. The Lindblad diagram illustrates the relationship between the Jacobi integral and the conservation of orbital circularity at corotation. The time derivative of equation A1 shows that changes in a star’s orbital angular momentum are linearly related to changes in its orbital energy with slope equal to the spiral pattern speed (represented by a dashed line in Figure A1). In a disc with a flat rotation curve, stars in circular orbits (solid curve) have logarithmically increasing orbital energy with linearly increasing orbital angular momentum, where vertical distance from this curve represents random orbital energy. At corotation (shown as an ‘X’ in Figure A1), the

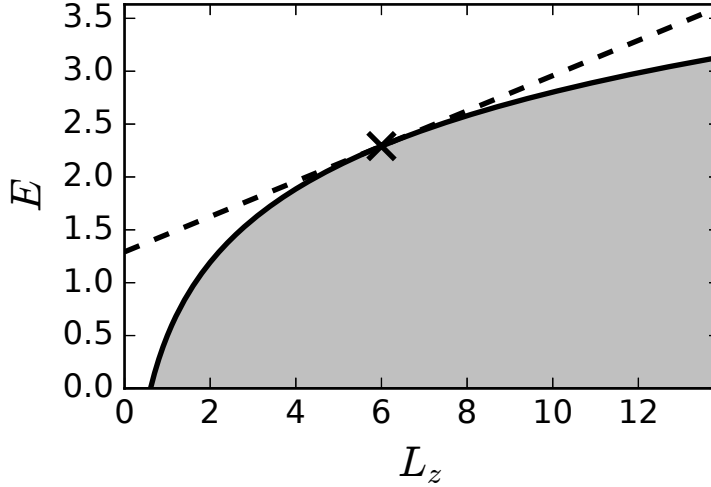


**Figure A1.** Lindblad diagram illustrating how changes in orbital angular momentum relate to changes in orbital energy via the Jacobi integral. The solid curve represents circular orbits and the shaded region is inaccessible since an orbit cannot have energy less than circular. Vertical distance from the solid curve represents random orbital energy. The ‘X’ marks corotation and the dashed line has slope equal to the pattern speed ( $\Omega_p$ ) of the spiral pattern. The Jacobi integral is conserved along lines with slope  $\Omega_p$ , so stars near corotation that have changes in orbital angular momentum will have little to no change in random orbital energy. This diagram uses units where  $v_c = L_z/R = 1$  and is only slightly modified from Figure 1 from Sellwood & Binney (2002).

slope of the line representing pattern speed is parallel to slope of constant orbital circularity. Since the Jacobi integral ( $E_J$ ) is conserved along lines with slope equal to the pattern speed ( $\Omega_p$ ), stars in trapped orbits do not have significant changes in orbital eccentricity with changes in orbital angular momentum around corotation.

The generalized capture criterion is derived using action variables, but in order to write an expression in terms of orbital energy and angular momentum we assume the epicyclic approximation. This approximation describes mildly non-circular orbits as simple harmonic oscillations about a circularly orbiting guiding centre. The epicyclic frequency of radial oscillations is given by (Binney & Tremaine 2008, equation 3.80),

$$\kappa^2(R_L) = \left( R \frac{d\Omega_c^2}{dR} + 4\Omega_c^2 \right)_{R_L}, \quad (\text{A3})$$

where  $\Omega_c$  is the circular orbital frequency, and the mean orbital radius<sup>18</sup> (i.e. “guiding centre radius”) is

$$R_L = R \frac{v_\phi}{v_c}. \quad (\text{A4})$$

The random orbital energy in the inertial frame is

$$E_{ran} = E - E_c(R_L), \quad (\text{A5})$$

where  $E_c(R)$  is the energy associated with a circular orbit in the underlying axisymmetric potential at radius  $R$ .

The form of the capture criterion appropriate for our assumed model is (Daniel & Wyse 2015, their equation 34)

$$-1 < \Lambda_{nc,2}(t) \leq 1, \quad (\text{A6})$$

where (Daniel & Wyse 2015, from their equations 11 & 33)

$$\Lambda_{nc,2}(t) \equiv \frac{E_J(R, \phi, v_R, v_\phi) - h_{CR}}{|\Phi_s|_{CR}} - \left( \frac{R_L(R, v_\phi, t)}{R_{CR}} \right) \left( \frac{E_{ran}(R, \phi, v_R, v_\phi, t)}{|\Phi_s|_{CR}} \right) \quad (\text{A7})$$

and  $h_{CR}$  is the Jacobi integral (equation A1) for a star at corotation in the underlying axisymmetric potential ( $\Phi_0(R_{CR})$ ).

<sup>18</sup> Note that this approximation is only strictly true for SHM, requiring radial oscillations be within a range where the surface density is approximately constant.